THE UNIVERSITY OF MANITOBA

EXPERIMENTAL ANALYSIS OF TURBULENT FLOW IN A LONGITUDINAL INTERNALLY FINNED TUBE

by

Albert Chun-Yau Lau

A Thesis

Submitted to the Faculty of Graduate Studies in

Partial Fulfillment of the Requirements for the

Degree of Master of Science

Department of Mechanical Engineering

Winnipeg, Manitoba
May, 1981

EXPERIMENTAL ANALYSIS OF TURBULENT FLOW IN A LONGITUDINAL INTERNALLY FINNED TUBE

BY

ALBERT CHUN-YAU LAU

A thesis submitted to the Faculty of Graduate Studies of the University of Manitoba in partial fulfillment of the requirements of the degree of

MASTER OF SCIENCE

ABSTRACT

An experimental study was conducted for fully developed turbulent air flow through a straight internally finned tube at Reynolds numbers (based on equivalent hydraulic diameter and axial bulk velocity) of 50,000 and 71,000. The finning configuration consisted of six longitudinal rectangular (38.1 x 4.9 mm) fins equi-spaced in a 114.3 mm I.D. tube. The 6.1 m long test section was installed on a wind tunnel which operated in the open circuit mode. Pitot tube and hot-wire anemometry measurements were made from the discharge end of the test section approximately 135 equivalent hydraulic diameter from the inlet.

Distributions of the mean axial velocity, when normalized by the bulk axial velocity, were independent of Reynolds number. Evidence in favor of an universal logarithmic law was found. Double peak velocities were found along the 30 degrees symmetry lines. Two counter-rotating cells of secondary flow were found to exist in each of the twelve primary flow cells, with a maximum secondary velocity of about 4½% of the bulk axial velocity. The average wall shear stress along the tube wall was almost the same as that along the fin surface. The effect of secondary flow was more pronounced upon the turbulent kinetic energy distribution than the axial mean velocity distribution. The experimental friction factor were about 5% to 8% higher than those predicted by the Prandtl-Nikuradse correlation.

TABLE OF CONTENTS

	Page
ABSTRACT	i
TABLE OF CONTENTS	ii
LIST OF FIGURES	iv
LIST OF TABLES	vi
NOMENCLATURE	vii
1.0 INTRODUCTION	1
1.1 Objective and Scope	2
2.0 THEORETICAL CONSIDERATIONS	4
3.0 LITERATURE REVIEW	8
3.1 Internally Finned Tubes	8
3.1.1 Laminar Flow	8
3.1.2 Turbulent Flow	9
3.2 Non-circular Ducts	13
3.3 Flow in Corners	16
4.0 EXPERIMENTAL FACILITY AND PROCEDURES	17
4.1 Wind Tunnel	17
4.2 Wind Tunnel Calibration	17
4.3 Test Section	18
4.4 Traversing Mechanism	19
4.5 Instrumentation	20
4.6 Experimental Procedures	21

Page

5.0 RESULTS AND DISCUSSION 24

5.1 General 24

5.2 Flow Development 24

5.3 Flow Symmetry 25

5.4 Friction Factor 26

5.5 Local Wall Shear Stress 27

5.6 Mean Axial Velocities 29

5.7 Secondary Flow 31

5.8 Reynolds Normal Stresses 33

5.9 Turbulent Kinetic Energy 34

5.10 Reynolds Shear Stresses 35

6.0 CONCLUDING REMARKS 36

7.0 ACKNOWLEDGEMENTS 37

8.0 REFERENCES 38

APPENDIX 42

TABLES 44

FIGURES 46

LIST OF FIGURES

Figures		Page
1	Wind Tunnel Layout	46
2	Wind Tunnel Calibration	47
3	Cross Section of Internally Finned Tube Test Section	48
4	Test Section	49
5	Internally Finned Tube Test Facility	50
6	Traversing Mechanism	50
7	θ-direction Traversing Mechanism	51
8	Sectional Drawing of the θ-direction Traversing Mechanism	52
9	Signal Process Circuit	53
10	Primary Flow Cell Grid Points	54
11	Radial Distribution of $\bar{U}$ in Primary Flow Cell I & II, Re = 71,000	55
12	Local Wall Shear Stress Distribution in Primary Flow Cell I & II Along the Tube Wall, Re = 71,000	56
13	Axial Static Pressure Distribution	57
14	Friction Factor vs Reynolds Number for the Internally Finned Tube	58
15	Local Wall Shear Stress Distributions	59
16	Isovels of $\bar{U}/U_b$, Re = 50,000	60
17	Isovels of $\bar{U}/U_b$, Re = 71,000	61
18	Radial Distributions of $\bar{U}/U_b$ in Primary Flow Cell, Re = 71,000	62

Figure		Page
19	u^+ vs y^+ (Tube).	63
20	u^+ vs y^+ (Fin), Re = 71,000	64
21	Circumferential Distribution of $\bar{V}$	65
22	Radial Distribution of $\bar{W}$ at θ = 25°	66
23	Radial Distribution of $\bar{W}$ at θ = 15°	67
24	Secondary Flow in the Primary Flow Cell, Re = 71,000	68
25	Radial Distribution of $\sqrt{\overline{u}^2}$ Along Symmetry Line (θ = 30°), Re = 71,000	69
26	Radial Distribution of $\sqrt{\overline{u^2}}$ in Primary Flow Cell, Re = 71,000	70
27	Radial Distribution of $\sqrt{\overline{v^2}}$ in Primary Flow Cell, Re = 71,000	71
28	Radial Distributions of $\sqrt{\overline{w^2}}$ in Primary Flow Cell, Re = 71,000	72
29	Turbulent Kinetic Energy	73
30	Radial Distribution of $\overline{uv}$ in Primary Flow Cell, Re = 71,000	74
31	Radial Distribution of $\overline{uw}$ in Primary Flow Cell, Re = 71,000	75
32	Radial Distribution of $\overline{uv}$, θ = 30°	76
33	Radial Distribution of $\overline{uv}$, θ = 25°	77
34	Radial Distribution of $\overline{uv}$, θ = 20°	78
35	Radial Distribution of $\overline{uv}$, θ = 15°	79
36	Radial Distribution of $\overline{uw}$, θ = 30°	80
37	Radial Distribution of $\overline{uw}$, θ = 25°	81
38	Radial Distribution of $\overline{uw}$, θ = 20°	82
39	Radial Distribution of $\overline{uw}$, θ = 15°	83

LIST OF TABLES

Table		Page
1	Turbulent Entrance Lengths for Various Types of Ducts	44
2	Empirical Constants for the Law of the Wall	45

NOMENCLATURE

a	radius of brass pipe
b	average distance between fins
d	outside diameter of Pitot tube
D_h	equivalent hydraulic diameter, 4 (cross-sectional area)/(actual wetted perimeter)
E_1	voltage of hot-wire with wire angle = + 45° to flow axis
E_2	voltage of hot-wire with wire angle = - 45° to flow axis
f	friction factor, $(2\ D_h/\rho U_{bt}^2)\ (dP/dx)$
H	dimensionless fin height, ℓ/R
L	length of test section
ℓ	fin height
M	number of equi-spaced fins
P	pressure
p	pitch of fins (length per turn)
$\bar{q}$	turbulent kinetic energy per unit mass, $\frac{1}{2}\ (\overline{u^2} + \overline{v^2} + \overline{w^2})$
r	radial distance from center of finned tube (radial coordinate)
R	inside radius of internally finned tube
Re	Reynolds number, $\rho U_{bt}\ D_h/\mu$
Re_b	Reynolds number, all fluid properties are based on bulk temperature $\rho U_{bt}\ D_h/\mu$
u, v, w	fluctuating components of the velocities in the axial, radial and peripheral directions, respectively
u^*	local friction velocity, $(\tau_w/\rho)^{\frac{1}{2}}$
$\overline{u^*}$	average friction velocity, $(\bar{\tau}/\rho)^{\frac{1}{2}}$

u^+	$\overline{U}/u^*$
$\bar{U}$	axial mean velocity (time-average)
U_b	average mean axial velocity over primary flow cell (bulk velocity)
U_{bt}	overall bulk velocity for internally finned tube
$\bar{U}_{sec}$	resultant of $\bar{V}$ and $\bar{W}$, $(\overline{V^2} + \overline{W^2})^{\frac{1}{2}}$
$\bar{V}$, $\bar{W}$	radial and peripheral mean velocities (secondary velocities)
x	axial coordinate
y, z	directions (see Fig. 3)
y^+	dimensionless distance from surface, (distance) u^*/ν
y^*	distance along fin measured from the fin tip
α	helix angle
θ	angular coordinate
ν	laminar kinematic viscosity
μ	laminar dynamic viscosity
ρ	fluid density
τ_w	local wall shear stress
$\bar{\tau}_w$	average of local wall shear stress over tube and fin
$\bar{\tau}$	average wall shear stress, (dP/dx) $(D_h/4)$

1.0 INTRODUCTION

In recent years, the need for high performance thermal systems has stimulated a considerable amount of research in methods to augment heat transfer. Usually at the expense of pumping power or external power applied to the systems, the techniques which have been found to enhance heat transfer for internal flows include:

1) displaced promoters, 2) surface vibration, 3) fluid vibration, 4) electrostatic fields, 5) fluid additives, 6) vortex flow, and 7) surface promoters. However, the methods 1 - 6 are either limited to certain size of system or not economically feasible. Surface promoters include: a) selective surface finish and b) increasing the heat transfer area by adding inner fins to the smooth tube. Many of the surface finishes are not feasible for mass-production from an economic standpoint. But adding inner fins to a smooth tube is a direct method of reducing the thermal resistance on the inside of the tubes.

Modern technology has recently made it possible to manufacture internally finned tubes. These have their application in heat exchange equipment; the most common arrangement being longitudinal fins of any shape attached to the inside peripheral surface of the tube. However, it is not possible to utilize data for the external fin or smooth pipe to predict the performance of these internally finned tubes. Several investigators [1 - 24] had studied the heat transfer and pressure drop characteristics of internally finned tubes in turbulent and laminar flow with different fluids. It was found that the performance of internally finned tubes was inherently superior to that of smooth pipe.

Internally finned tubes can also be classified in the category of non-circular ducts. Turbulent flow in such a geometry is accompanied by lateral spiral motions. These spiral motions, called secondary flows, convect primary flow momentum towards the walls in some region and away from the walls in other regions. The secondary flows can affect the temperature distribution and consequently the heat transfer performance of internally finned tubes. So far, no detailed measurements of primary flow and secondary flows are available for internally finned tubes.

1.1 Objective and Scope

The present work was done to explore experimentally the flow structure of fully developed turbulent adiabatic air flow through an internally finned tube. The experimental results had also served as a basis for a two-equation turbulence model which had been developed* to predict both fluid flow and heat transfer characteristics in internally finned tubes under fully developed conditions. The test section shown in Fig. 1 was installed on a wind tunnel which operated in the open circuit mode. Following confirmation of flow symmetry, the Pitot tube and hot-wire anemometry measurements were made in one of the twelve primary flow cells.

In order to facilitate measurements, the cross section of the test section should be as large as possible; however, the test section size was limited by the capacity of the existing wind tunnel. The

*M.N.A. Said: Ph.D. Thesis Project

dimensions of the finned tube test section are $M = 6$, $H = 0.667$, $D_h = 44.8$ mm, $L = 6.1$ m and $R = 57.15$ mm.

For the sake of scaling, the measurement of local wall stress distribution, axial mean velocity, secondary velocity and Reynolds stresses were made at Reynolds numbers of 50,000 and 71,000.

2.0 THEORETICAL CONSIDERATION

The cross-sectional view of the test section is shown in Fig. 3. The flow cross-section is symmetric in twelve parts; each part forming a primary flow cell. The primary flow cell under study was primary flow cell I shown in Fig. 3.

For fully developed turbulent flow of an incompressible, isothermal fluid through a primary flow cell, the equations of motion in cylindrical polar coordinate system (x, r, θ) are:

Axial direction:

$$V \frac{\partial U}{\partial r} + \frac{W}{r}\frac{\partial U}{\partial \theta} = -\frac{1}{\rho}\frac{\partial P}{\partial x} + \nu \nabla^2 U \qquad (1)$$

Radial direction;

$$V \frac{\partial V}{\partial r} + \frac{W}{r}\frac{\partial V}{\partial \theta} - \frac{W^2}{r} = -\frac{1}{\rho}\frac{\partial P}{\partial r} + \nu \left(\nabla^2 V - \frac{V}{r^2} - \frac{2}{r^2}\frac{\partial W}{\partial \theta}\right) \qquad (2)$$

Peripheral direction:

$$V \frac{\partial W}{\partial r} + \frac{W}{r}\frac{\partial W}{\partial \theta} + \frac{VW}{r} = -\frac{1}{\rho}\frac{1}{r}\frac{\partial P}{\partial \theta} + \nu \left(\nabla^2 W - \frac{W}{r^2} + \frac{2}{r^2}\frac{\partial W}{\partial \theta}\right) \qquad (3)$$

where

$$\nabla^2 = \frac{\partial^2}{\partial x^2} + \frac{\partial^2}{\partial r^2} + \frac{1}{r}\frac{\partial}{\partial r} + \frac{1}{r^2}\frac{\partial^2}{\partial \theta^2}$$

$$U = \bar{U} + u$$

$$V = \bar{V} + v$$

$$W = \bar{W} + w$$

$$P = \bar{P} + p'$$

The continuity equations representing conservation of mass are:

$$\frac{\partial U}{\partial x} + \frac{1}{r}\frac{\partial (rV)}{\partial r} + \frac{1}{r}\frac{\partial W}{\partial \theta} = 0 \tag{4}$$

$$\frac{1}{r}\frac{\partial (r\bar{V})}{\partial r} + \frac{1}{r}\frac{\partial \bar{W}}{\partial \theta} = 0 \tag{5}$$

$$\frac{\partial u}{\partial x} + \frac{1}{r}\frac{\partial (rv)}{\partial r} + \frac{1}{r}\frac{\partial w}{\partial \theta} = 0 \quad . \tag{6}$$

The Reynolds equations are:

Axial direction:

$$\bar{V}\frac{\partial \bar{U}}{\partial r} + \frac{\bar{W}}{r}\frac{\partial \bar{U}}{\partial \theta} = -\frac{1}{\rho}\frac{\partial \bar{P}}{\partial x} - \left[\frac{1}{r}\frac{\partial (r\overline{uv})}{\partial r} + \frac{1}{r}\frac{\partial (\overline{uw})}{\partial \theta}\right]$$
$$+ \nu\left[\frac{\partial^2 \bar{U}}{\partial r^2} + \frac{1}{r}\frac{\partial \bar{U}}{\partial r} + \frac{1}{r^2}\frac{\partial^2 \bar{U}}{\partial \theta^2}\right] \tag{7}$$

Radial direction:

$$\bar{V}\frac{\partial \bar{V}}{\partial r} + \frac{\bar{W}}{r}\frac{\partial \bar{V}}{\partial \theta} - \frac{\bar{W}^2}{r} = -\frac{1}{\rho}\frac{\partial \bar{P}}{\partial r} - \left[\frac{1}{r}\frac{\partial (r\overline{v^2})}{\partial r}\right.$$
$$\left. + \frac{1}{r}\frac{\partial (\overline{vw})}{\partial \theta} - \frac{\overline{w^2}}{r}\right] + \nu\left[\frac{\partial^2 \bar{V}}{\partial r^2} + \frac{1}{r}\frac{\partial \bar{V}}{\partial r} + \right.$$
$$\left.\frac{1}{r^2}\frac{\partial^2 \bar{V}}{\partial \theta^2} - \frac{\bar{V}}{r^2} - \frac{2}{r^2}\frac{\partial \bar{W}}{\partial \theta}\right] \tag{8}$$

<u>Peripheral direction:</u>

$$\bar{V}\frac{\partial \bar{W}}{\partial r} + \frac{\bar{W}}{r}\frac{\partial \bar{W}}{\partial \theta} + \frac{\bar{V}\bar{W}}{r} = -\frac{1}{\rho r}\frac{\partial \bar{P}}{\partial \theta} -$$

$$\left[\frac{\partial(\overline{vw})}{\partial r} + \frac{1}{r}\frac{\partial \overline{w^2}}{\partial \theta} + 2\frac{\overline{vw}}{r}\right] + \nu$$

$$\left[\frac{\partial^2 \bar{W}}{\partial r^2} + \frac{1}{r}\frac{\partial \bar{W}}{\partial r} + \frac{1}{r^2}\frac{\partial^2 \bar{W}}{\partial \theta^2} + \frac{2}{r^2}\frac{\partial \bar{V}}{\partial \theta} - \frac{\bar{W}}{r^2}\right] \quad . \tag{9}$$

The boundary conditions are:

1) Due to no-slip condition at the solid boundary

$U = V = W = 0$ for all θ and y^*

2) Due to symmetry

$\frac{\partial \bar{U}}{\partial r} = 0 = \bar{V} = \bar{W}$ at $r = 0$

Concerning the symmetry lines, $\theta = 0$ and $\frac{\pi}{6}$

3) Since secondary flow cannot cross the symmetry lines

$\bar{W} = 0 = \frac{\partial \bar{W}}{\partial r} = \frac{\partial^2 \bar{W}}{\partial r^2}$

4) Due to symmetry

$\frac{1}{r}\frac{\partial \bar{P}}{\partial \theta} = 0$

5) Since $\bar{W}$ has opposite signs on each side of a symmetry line

$$\frac{1}{r^2}\frac{\partial^2\bar{W}}{\partial\theta^2} = 0 \ .$$

At the cell boundaries (or symmetry lines), the Reynolds equations become:

$$0 = -\bar{V}\frac{\partial\bar{U}}{\partial r} - \frac{1}{\rho}\frac{\partial\bar{P}}{\partial x} - \frac{1}{r}\frac{\partial(r\overline{uv})}{\partial r} - \frac{1}{r}\frac{\partial(\overline{uw})}{\partial\theta}$$

$$+ \nu\left[\frac{1}{r}\frac{\partial}{\partial r}\left(r\frac{\partial U}{\partial r}\right)\right] \tag{10}$$

$$0 = -\bar{V}\frac{\partial\bar{V}}{\partial r} - \frac{1}{\rho}\frac{\partial\bar{P}}{\partial r} - \frac{1}{r}\frac{\partial(r\overline{v^2})}{\partial r} - \frac{\overline{w^2}}{r}$$

$$+ \nu\left[\frac{1}{r}\frac{\partial}{\partial r}\left(r\frac{\partial\bar{V}}{\partial r}\right) - \frac{\bar{V}}{r^2}\right] \tag{11}$$

$$0 = \frac{\partial(\overline{vw})}{\partial r} + 2\,\frac{\overline{vw}}{r} \ . \tag{12}$$

Equation (12) must vanish since there is no net momentum transfer in the peripheral direction. By integrating equation (12) and using the boundary condition $\overline{vw} = 0$ at $r = R$, it follows that $\overline{vw} = 0$ for all values of r. However, it is not possible to reduce equations (10) and (11) any further because both $\bar{V}$ and $\frac{1}{r}\frac{\partial\overline{uw}}{\partial\theta}$ may be non-zero since $\frac{1}{r}\frac{\partial\overline{uw}}{\partial\theta}$ have finite values due to the asymmetric distribution of $\overline{uw}$.

3.0 LITERATURE SURVEY

The available publication on turbulence characteristics in internally finned tube is very scarce. In the following sections, literature on fluid flow and heat transfer characteristics of internally finned tubes, secondary flow in non-circular ducts and flow in corners are reviewed.

3.1 Internally Finned Tubes

A survey of publications shows an abundance of experimental and analytical studies on fluid flow and heat transfer performance of internally finned tubes in both laminar and turbulent flow.

3.1.1 Laminar flow

Regarding experimental results, Vasilchenko & Barbaritskaya [1, 2], Watkinson et al [3], Soliman & Feingold [4] and Marner & Bergles [5] studied both fluid flow and heat transfer characteristics of internally finned tubes (straight or spiral fins) and found that the heat transfer performance of finned tubes were much superior to smooth tubes.

In regard to analytical studies, Hu & Chang [6] investigated the heat transfer of fully developed laminar flow with zero fin thickness under axially uniform heat flux. Taking into account fin thickness, Masliyah & Nandakumar [7] obtained a solution for temperature distribution by using the finite element method. Soliman & Feingold [8] developed an infinite series solution for velocity distribution and friction factor. For internally finned tubes with long fins, secondary loops were found to exist within the inter-fin region. Later, Soliman & Feingold [9] obtained the analytical solution for temperature distribution and Nusselt numbers for uniform heat input axially and peripherally uniform inside wall temperature. For various combinations of fin height and thickness, it was found that the Nusselt number (based on inside tube diameter) increased with the increase of M upto a critical M beyond which a reversal of trend occurred. Later, Soliman [10] included the effect of fin conductance. Under axial uniform heat flux and constant outside wall temperature, the heat transfer characteristics were influenced by the product of fin half-angle and the ratio of thermal conductivity of fin material to that of the fluid.

3.1.2 Turbulent flow

Experiments on internally finned tubes in turbulent flow have been done extensively over a wide range of number of fins and fin patterns.

Brouillette et al [11] investigated the heat transfer and pressure drop performance of tubes which had 60° V-shaped notches on the inner surface. The relative roughness of these tubes varied from .009 to .050. It was found that, at Reynolds number (based on average inside diameter of finned tube) from 30,000 to 175,000 , high relative roughness enhanced the heat transfer performance significantly. Increasing either the relative roughness or number of fins increased the pressure drop.

Covering Re_b from 1,000 to 20,000, Hilding & Coogan [12] found that the internally finned tubes (M = 4 - 8) had marked heat transfer improvement in the laminar and transition region only.

Lipets et al [13] tested internally finned tubes (M = 8 - 11, D_h = 14 - 37 mm) under industrial conditions. When arranged in a staggered array in a superheater of a commercial boiler, the wall temperature of the finned tubes was found to be 24°C and 15°C lower than for smooth tubes in the first and third row respectively.

Ornatskii et al [14] investigated the mean velocity distributions in the obstructed part of the cross section of the tube and the space between the fins. Turbulent flow was observed to exist in the main flow and concurrentflow simultaneously; however, the degrees of turbulence were different. It was observed that the velocity distribution had no Reynolds number dependence when normalized by the axial mean velocity. Unlike the velocity distribution in the main flow region, the velocity distribution in the inter-fin space was substantially influenced by b/ℓ.

Bergles et al [15] investigated the heat transfer performance of tubes with straight and spiral fins (M = 10 - 30, H = 0.1-0.48, p/2R = 5.69 - 123.0) at Re_b from 1,000 to 40,000. It was found that short spiral fin tubes provided the optimal heat transfer enhancement.

Covering Re_b from 10,000 to 150,000, Watkinson et al [16, 17] investigated the heat transfer and pressure drop of internally finned tubes (M = 6 - 50, H =0.198 -0.516, p/2R = 6 - 21) with water and air.

Using the heat transfer performance of smooth tube for comparison, the Nusselt number (based on effective area and equivalent hydraulic diameter) for straight fin tubes increased with b/D_h and the Nusselt number for spiral fin tubes decreased with increasing p/D_h. However, the enhancement for water was more than for air.

Russell & Carnavos [18] tested longitudinal internally finned tubes (M = 10, I.D. = 7.04 - 15.7 mm) in turbulent air flow. The Reynolds numbers (based on I.D.) were from 10,000 to 500,000. It is found that heat transfer enhancement over the smooth tube values was equal to the increased heat transfer area. The increase in friction was from 80% to 100% of the square of the increased heat transfer area. Smaller diameter finned tubes would result in higher transfer enhancement.

Carnavos [19] found that total footage required could be reduced by 17% to 100% when using finned tubes with straight or spiral fins ($M = 6 - 41$, $H = 0.05 - 0.58$, $\alpha = 2.5° - 20°$) instead of smooth tube. When testing the same finned tubes with water and ethylene-glycol/water solution instead of air, Carnavos [20] observed that the heat transfer performance of finned tubes had the same Prandtl number dependence as a smooth tube.

Ivanovic [21] developed both a turbulent mixing length model and a low Reynolds number model to predict the characteristics of flow and heat transfer for straight finned tubes with $6 \leq M \leq 18$ and $0.2 \leq H \leq 0.45$. Even with zero thickness fin and neglect of secondary flows, the numerical predictions of Nusselt number and friction factor were in good agreement with the published experimental results.

Minchenko & Shvartsman [22] obtained the optimal dimensions of helically finned tube for any thermal conditions at any pressure. After installing this tube in the steam generator, it was found that the best thermal efficiency was in both sub-critical and super-critical pressure.

Gee & Webb [23] reported that the helically ribbed tubes (p/ℓ = 15, α = 30°, 49° and 70°) yield greater heat transfer per unit pumping power than traversely ribbed tubes. The preferred helix angle was approximately 49°.

Royal & Bergles [24] studied the condensation of low pressure steam inside horizontal tubes of different internal geometries which consisted of a smooth tube having two twisted tapes inserts and four internally finned tubes (three with twisted fins and one with straight fins, $M = 6 - 32$, $p/2R = 3.3 - 20.7$). Based on nominal area, twisted-tape inserts were found to increase the average heat transfer coefficient of condensating steam by as much as 30% above smooth tube values. The best performing internally finned tube increased in-tube condensation heat transfer coefficient by as much as 150% above the smooth tube values.

3.2 Non-Circular Ducts

Turbulent flow in a non-circular duct is accompanied by lateral spiral motions. This spiral motion, called secondary flow, is generated to maintain equilibrium by the Reynolds stresses and pressure gradients in the plane normal to the axial direction. Secondary flows exist in many geometries such as square and rectangular ducts, triangular ducts, eccentric annulus, and parallel flow rod bundles. The square and rectangular ducts and parallel flow rod bundles have been studied the most extensively both experimentally and analytically.

In 1926, Nikuradse delineated the difference between flow in circular pipes and square ducts. Isovels bulged towards the corners and were lifted away from the midpoint of the walls. In 1927, Prandtl suggested these were the result of secondary flows towards the corners which required a return flow at the midpoint of the walls to satisfy continuity. Prandtl suggested that the asymmetry of the turbulent stresses provided the cause of the secondary flow. Alternatively, secondary flow might be caused by a traverse wall shear stress gradient. Prior to the work of Hoagland, direct measurement of the secondary velocities was impossible due to the error introduced by the presence of the yaw-meter when used in regions possessing steep mean axial velocity gradients. Since the typical magnitude of secondary velocities is only a few percent of the primary velocity, any small distortions of the flow caused by the measuring probe could have an appreciable effect on secondary velocity measurements.

Hoagland's work was a major accomplishment of the hot-wire probe technique. Hoagland [25] found that the flow pattern was that predicted by Prandtl. The secondary flow generally was confined to the corner region and maximum secondary velocity having magnitude of 1.5% of the axial centerline velocity was found along the wall near the corners. Leutheusser[26] reported that the inner law of the wall was applicable after adjusting the constants to compensate for the duct geometry. Friction coefficients for rectangular ducts were different from those for circular pipe. Through experimental evaluation of terms in the axial vorticity equation, Brundrett and Baines [27] showed that convection and diffusion of secondary flow vorticity were balanced approximately by the production of vorticity from the Reynolds stresses. Gessner and Jones [28] concluded that, when examining the Reynolds equation along a secondary flow streamline, secondary flows must be the result of forces exerted by static pressure gradients and the Reynolds stresses in plane normal to the primary flow direction. Launder and Ying[29] measured secondary velocities in both rough wall and smooth wall square ducts. They reported that friction velocity was a better scaling factor for the secondary velocities than axial bulk velocity because secondary velocities normalized with friction velocity were effectively independent of Reynolds number.

Kacker [30] conducted an experimental study of fully developed turbulent flow in a circular pipe containing one or two rods located off center. For the single pin geometry, one circulating secondary flow cell was found to exist in each symmetric half of the geometry. Two counter-rotating flow cells were found to exist within each of the quadrants for the double pin geometry. There was a smaller flow cell, which was nearly 60% of the flow in the larger cell, sandwiched between the center of the pipe and the half pin.

Lyall [31] investigated the turbulent flow characteristics in interconnected subchannels. Distribution of primary flow and secondary flow were obtained for two configurations, namely the interconnected gap between the subchannels was either fully open or half closed. For both configurations peak secondary velocity of 3.5% of the local primary velocity was found near the gap. The flow distribution indicated a significant momentum transfer from the larger to the smaller subchannel via the interconnecting gap.

Aly et al [32] found, for an equilateral triangular duct,that the secondary flow pattern consisted of six counter-rotating cells bounded by the corner bisectors. The effect of secondary flows on the turbulent kinetic energy field was more pronounced than on the axial mean velocity field.

Ambient secondary flow patterns depend on the duct geometry. For square ducts and equilateral triangular ducts, there is one cell per primary flow cell, but there exists more than one cell per primary flow cell for eccentric annulus, isosceles triangular ducts and rectangular ducts, etc. For internally finned tubes, fin height is expected to have a substantial influence on the secondary flow pattern.

For instance, for fixed M, if H = 1, secondary flow pattern might be similar to that of an isosceles triangular duct, i.e., three counter-rotating cells per primary flow cell. Secondary flow pattern will become two cells for a certain fin height ($0 < H < 1$). Secondary flow is non-existant for extremely short fin ($H \sim 0$).

3.3 Flow in Corners

Literature on flow near a corner region is very limited. In contrast to the turbulent corner flow, Zamir & Young [33] found, in a laminar corner flow, that the secondary flow was one of flows towards the corner close to the plate surfaces and outwards from the corner in the plane of symmetry.

Regarding the applicability of the universal law, no specific literature was found for the corner region, however data such as [26] suggest that the universal law of the wall holds fairly well for orthogonal walls.

4.0 EXPERIMENTAL FACILITY AND PROCEDURES

4.1 Wind Tunnel

The wind tunnel portion of the present facility was that used previously by Gerrard [34] in his flow investigation of the equilateral triangular duct. For the present work, the wind tunnel was operated in the open circuit mode. As shown in Fig. 1, following the fan section, air passed through a diffuser, two sets of turning vanes, a screen section and a circular contraction cone before entering a transition section. In this section, the flow area was gradually reduced to match the diameter of test section. Air discharged from the open end of the test section.

4.2 Wind Tunnel Calibration

The wind tunnel was calibrated for mass flow rate ($\dot{m}$) against the pressure drop across the contraction cone (ΔP). Calibration was done by operating the wind tunnel in the open circuit mode with a 2.67 m long, 0.27 m I.D. smooth brass pipe attached to the contraction cone (component 13 in Fig. 1). The pressure drop across the contraction cone was measured by using an Airflow Development Ltd. 0 - 0.5 in. water gauge manometer. In conjunction with a Betz manometer, local axial velocity U_r was measured at a number of radii by using a standard Pitot-static tube (O.D. 1.24 mm, manufactured by United Sensor and Control Corp., U.S.A.). The bulk velocity was evaluated by integrating the integral $\int_0^a U_r\, r\, dr$ or $U_{bt}\frac{a^2}{2}$ graphically, namely the area under the resulting curve of the plot of $U_r r$ against r. Then the mass flow rate was calculated from the continuity equation. The wind tunnel calibration curve is shown in Fig. 2.

4.3 Test Section

The internally finned tube test section consisted of two 3.05 m long test sections, the finning configuration consisted of six straight fins equi-spaced in a 114.3 mm I.D. tube. The tube for the test section was Ohio & Regal honed hydraulic tubing (nominal 127 mm O.D. x 6.35 mm wall type 1020 steel) which had internal surface finish of about 0.51 micrometer R.M.S. The tube inside diameter was found to be essentially uniform at 114.3 mm. The fins were made from type 1020 cold finished steel flats. Typical dimensions of the fin cross-section were a thickness of 4.88 $\pm$ 0.10 mm and a fin height of 38.1 $\pm$ 0.10 mm. Holes were drilled through the tube wall along the axial direction; each fin which was centrally tapped was fastened to the inner surface of the tube wall using hollow head screws. Before installed to the tubing, each fin was straightened and polished by emery paper - 400 and 600.

Test Section A (see Figs. 4 and 5) was flanged to the nozzle and the other end was joined to Test Section B by a keyed collar which assured alignment of the fins in the two sections.

The provision for axial static pressure measurements were made by locating static pressure taps at 152.4 mm interval along the Test Section B. Three static pressure taps were equi-spaced around the circumference of the tube.

Pitot tube and hot-wire anemometry measurements are made at 30 mm inside the discharge end of the Test Section B or namely at 135 D_h from the inlet.

4.4 Traversing Mechanism (Figs. 6-8)

The Traversing Mechanism used provided measurements on a cylindrical coordinate system (r, θ) basis.

The θ-direction traversing mechanism consisted of the following essential parts: circular brass plate carrying a circular graduated arc (originally from a Vernier Theodolite) was attached to a tube concentrically. The center of this brass plate was bored out to form a bearing for a shaft. A steel disk was fitted into the hollow part of the brass plate which enabled it to rotate freely and concentrically. The disk was attached to a shaft which worked in the bearing.

A vernier was mounted on the rim of the steel disk; this veriner enabled fine readings to be taken on the graduated arc. As shown in Fig. 7a, two sets of double-row-arranged holes were drilled through both the steel disk and brass plate at intervals of 5 degrees. Angular positioning was made by rotating the steel disk and then inserting dowel pins into these holes. Besides inserting dowel pins, the angular positioning could be locked into position by fastening a nut to the last portion of the shaft. As seen in Fig. 7b, the entire θ-direction traversing mechanism was held up by two brackets which were in turn supported by four threaded rods. These four threaded rods allowed the mechanism to move in the Z (vertical) direction.

The precise vertical motion was achieved by means of a DISA 55H01 traversing mechanism. This mechanism was mounted on two vernier calipers which allowed 15 cm travel in the r direction. The r-Z direction traversing mechanism was mounted on an aluminum square plate which was attached to the steel disk of θ-direction traversing mechanism.

As shown in Fig. 6, the entire assembly was mounted on a milling table which allowed a 37.5 cm and 16.6 cm movement in the x (longitudinal) and y (lateral) direction.

Regarding positioning accuracy, the movement was within 0.0254 mm and 1 minute for r and θ direction respectively. Eccentricity was negligible over the rotation of 90 degrees.

4.5 Instrumentation

Mean axial velocity and wall shear stress measurements were made using a Pitot tube and a Betz manometer. The Pitot tube had an outside diameter of 1.27 mm and was constructed from stainless steel tubing having an inside to outside diameter ratio of 0.6. The Betz manometer which was also used for axial pressure drop measurements had a range 0 - 400 mm water and an accuracy of $\pm$ 0.05 mm water.

Turbulence measurements were made using constant temperature linearized hot-wire anemometry manufactured by DISA. This system consisted of a 55M01 anemometer and a 55M25 linearizer and was operated in conjunction with DISA hot-wire probe having 1.25 mm sensor length of 5 μm diameter platinum-plated tungsten wire. The hot-wire probes included a 55P11 single wire, a 55P61 X-probe and a 55P12 45° slanting probe. Before being used for actual measurements, each probe was calibrated daily using DISA 55D90 calibration equipment. Most of the measurements ($\bar{V}$, $\bar{W}$, $\overline{u^2}$, $\overline{v^2}$, $\overline{w^2}$, $\overline{uv}$ and $\overline{uw}$) were made using the X-probe in the u, v and u, w mode. The single wire probe was used for $\bar{U}$ and $\overline{u^2}$ measurements, whereas the 45° slanting probe was used to measure the secondary velocities at Reynolds number of 71,000. Fig. 9 illustrates the set-up for the X-probe signal processing circuit. The experimental data were corrected for tangential cooling effects as suggested by Lawn [35]. The required corrections are summarized in Fig. 9; k was taken as 0.23 for DISA probe.

4.6 Experimental Procedures

Initial positioning of probe at the tube centerline was an essential step of the experimentation because all the measurements were begun at this reference point. Locating the tube centerline was accomplished by visual alignment with the aid of a paper overlay which had an exact geometry of the finned tube cross section. The measuring probe was moved (with $\theta = 0$) to the tube centerline using a DISA 55H01 traversing mechanism which was then locked into position. Thereafter, movement in the r-direction was over two vernier calipers, while θ movement was obtained by rotating the entire assembly via the θ-direction traversing mechanism.

For the X-probe technique, the channels of X-probe were initially calibrated and matched on the calibration equipment. The probe was aligned visually in either the x-r plane for $\bar{V}$ and $\overline{uv}$ or the x-θ plane for $\bar{W}$ and $\overline{uw}$. Then the procedures for measuring secondary velocities and Reynolds stresses were as follows:

1) The probe was located at the tube centerline where $\bar{V} = 0 = \bar{W}$ and $\frac{\partial \bar{U}}{\partial r} = 0$.

2) The two channels were checked for match; a difference in voltage was an indication of either the probe was not exactly at the tube centerline or the probe was not aligned in the plane of interest. If necessary, the probe was moved to the centerline and/or was rotated in its plane until the voltage difference was zero. Then AC and DC signals were recorded.

3) With θ fixed, a radial traverse was begun and measurement was made at each grid point.

4) At the end of the traverse, the probe was returned to the tube centerline to assure that the channels had not drifted.

5) The two channels were matched via linearized gain if necessary. As a further check, step 3 was repeated with the order of grid points reversed. Otherwise, a second radial traverse with new θ was started. All measurements were made in the manner described above.

The slant 45° probe technique was somewhat similar to that of X-probe. The slant 45° probe was aligned with the axial mean flow direction. Initially the probe was positioned at the tube centerline with wire angle of 45°; the voltage output E_1 were made rapidly along a radial traverse. At the end of the traverse, the probe was travelled back to the tube centerline to check whether the voltage reading had changed or not. The adjustment was made via linearizer gain if necessary.

The probe was rotated 180° about its axis; so that the wire angle was - 45°. In order to assure that the axis of rotation of the probe was aligned with the tube axis, the probe was removed from the probe holder, then rotated 180° and reinstalled with its reverse polarity. It was accustomed to adjust the channel to give the same DC and AC signals if necessary. Similarly, a second radial traverse were made along the same radial line to obtain local voltage output E_2. The corresponding local secondary velocity was computed using the same equation as for the X-probe as shown in Fig. 9.

5.0 RESULTS AND DISCUSSIONS

5.1 General

All basic fully developed flow measurements were made at the grid points shown in Fig. 10. There are 69 measurement locations for the Pitot tube while the single wire probe (or X-probe) had 65 (or 62) stations. Within each primary flow cell, the free flow area was divided into two regions: a) central core region, $0 \leq r/R \leq .33$ for all θ; b) inter-fin region, $.33 \leq r/R \leq 1$ for all θ. Most of the experimental data presented have been normalized by either U_b or $\overline{u^*}$. Four sets of flow measurements were conducted at each Reynolds number. The corrections used and the error analysis are presented in the Appendix.

Detailed experimental data has been documented in Internal Report ER25.30, Department of Mechanical Engineering, University of Manitoba.

5.2 Flow Development

The test section had an overall length of 136 hydraulic diameters (D_h = .0448 m) for flow development. The usual criterion for fully developed flow is $L/D_h > 40$ for circular pipe. As shown in Table 1, fully developed turbulent flow have been achieved in non-circular ducts shorter than 136 D_h. Ornatskii et al [14] claimed that fully developed flow was achieved in finned tube segment channel with L/D_h from 30 to 40.

Before undertaking detailed measurements, a series of investigations were conducted to ensure the flow was fully developed at the measuring station. Axial pressure drop measurements were obtained for seven Reynolds numbers; the maximum percentage difference of axial pressure gradient at the length of 90 D_h and 130 D_h was 1%. As shown in Fig. 13, it was observed that the pressure decreased linearly with axial distance beyond $L/D_h \approx 70$.

Centerline velocity was measure via Pitot-static tube beginning at the exit of the discharge end of the test section. The Pitot-static tube was advanced upstream into the test section upto 80 mm. Beyond 15 mm from the open end, the centerline velocity became constant. It was evidenced that the end effect penetrated only 15 mm.

In view of the above review and observations, it could be safely assumed that the flow was fully developed at the measuring station.

5.3 Flow Symmetry

Axial velocity measurements were obtained via Pitot tube along radial lines at $\theta = 15°$ and $30°$ for primary flow cell I, and at all apparent symmetric points in primary flow cell II. Also, the wall shear stress distributions were obtained via Preston tube along the tube wall for primary flow cell I and II. The axial velocity measurements are shown in Fig. 11. The maximum deviation is about 3% at $r/R = 0.33$, $\theta = 15°$. As seen in Fig. 12, the wall shear stress distributions are essentially a single distribution for primary flow cells I and II.

According to the axial velocities and wall shear stress measurements, it was concluded the flow structure in the primary flow cell I was reasonably symmetric with its immediate neighbouring flow cells. Henceforth, the Pitot tube and hot-wire anemometry measurements were concentrated in one of the twelve primary flow cells, namely primary flow cell I.

5.4 Friction Factor

The axial pressure distributions at Reynolds numbers of 50,000 and 71,000 were determined from measurements at 19 static pressure taps/piezometer rings spanning the last 3.05 m of the test section. Referred to the static pressure at L/D_h = 133, the normalized distributions are shown in Fig. 13 where the straight lines represent the lines faired through the data. No marked entrance region is evident. As expected, pressure decreases linearly with axial distance.

Subsequently, pressure drop measurements were made at 10 different mass flow rates, covering Reynolds number from 35,000 to 71,000. After determining the axial pressure gradient via least-square-fit to the data, the friction factors were computed as $D_h\ (-dP/dx)/\frac{1}{2}\rho U_{bt}^{\ 2}$. As shown in Fig. 14 (f vs Re), the data shows the usual trend of f decreased with increasing Re. Friction factors were found to be about 5% - 8% higher than those predicted by the Prandtl-Nikuradse equation. This discrepency may be due to the fact that the equivalent hydraulic diameter concept is not sufficient to rationalize the geometry difference between the pipe and internally finned tube.

Fig. 14 also shows the correlation of friction factor of Watkinson et al [17]. This correlation for turbulent air flow through straight finned tube is:

$$f = 0.524 \left(\frac{b}{D_h}\right)^{0.17} (Re)^{-0.29} \qquad \begin{array}{l} 7{,}500 < Re < 75{,}000 \\ 0.2 \leq (b/D_h) \leq 0.5 \end{array}$$

where b is the average distance between fins. The distance b was calculated as the arithmetic mean of the circumferential distance between two adjacent fins at the fin root and at the fin tip. The (b/D_h) ratio was 0.781 and hence somewhat beyond the prescribed range of [17]. However, the present data lies only slightly above the correlation in [17] by about 3.5%. Also, comparing with the correlation of Carnavos [20], the results were found to be about 10% higher. These are due to the fact that the adiabatic results are generally higher than the diabatic results. The difference in tube geometry may also cause this difference in friction factors.

5.5 Local Wall Shear Stress

Assuming the universality of the law of the wall regardless of the geometry of the duct, the Preston tube technique was applied to determine the local wall shear stress distribution. A round tipped Pitot tube with O.D. of 1.27 mm was placed in direct contact with the tube wall (or fin surface) of primary flow cell I. The Preston tube reading was the difference between Pitot and static pressure at 30 mm from the discharge end of the test section. The magnitudes of the axial wall shear stress were calculated from the correlation of Patel

[36]. According to Patel [36], the experimental calibration is valid up to $u^* d/\nu$ values of 1270. In the present work, the maximum value of $u^* d/\nu$ was 117.75 which was below this upper limit.

Including the local wall shear stress at the fin tip, the integrated average wall shear stress ($\bar{\tau}_w$) was higher than the average values ($\bar{\tau}$) obtained from axial pressure gradient by 4% and 6% for Re = 50,000 and 71,000 respectively. This discrepancy may be due to inaccuracy in the wall shear stress measurements. The normalized (by $\bar{\tau}_w$) distributions shown in Fig. 15 are considered to be fairly accurate except perhaps for the corner region.

The distribution of the wall stress along the solid boundary was normalized by integrated average shear stress ($\bar{\tau}_w$). As shown in Fig. 15, the shear stress distribution is independent of Reynolds number. These distributions are fairly flat ($0.9 < \tau_w/\bar{\tau}_w < 1.1$) between 8° and 30° for the tube wall and between $y^*/\ell = 0.2$ and 0.8 for the fin surface. The wall shear stress at the fin tip was found higher than that at $y^*/\ell = 0$, about 11% for Re = 50,000 and about 12% for Re = 71,000. This indicates that there are high velocity gradients near the fin tip. Along the wall and fin, the shear stresses decreased towards the corner region. The average wall shear stress along the wall was 4% and 3% lower than that along the fin surface for Re = 50,000 and 71,000 respectively. This trend was evidence that the secondary flows tended to equalize the shear stress distribution.

5.6 Mean Axial Velocities

Mean axial velocity distributions within the primary flow cell were measured by Pitot tube and single wire probe at Reynolds number of 50,000 and 71,000. All velocity calculations were based on actual air properties in the wind tunnel and density correction due to daily relative humidity variations. The results from these two measurement techniques were consistent. The Pitot tube data were considered accurate to within 1%.

The isovels presented in Figs. 16 and 17 have been normalized by bulk velocity U_b which was obtained by numerical integration of experimental local velocities. These U_b values from the Pitot tube measurements were in good agreement with the bulk velocities for the entire tube (U_{bt}) as determined via contraction cone pressure drop. In the central core region, the isovels are bulging away from the fin tip, while the isovels are bulging towards the corner in the inter-fin region. These velocity distribution exhibits disturbances which can be attributed to secondary flows. As shown in Figs. 16, 17 and 18, there are two maximum velocities along the symmetry line ($\theta = 30°$); the absolute maximum velocity is located at the tube centerline and the second maximum velocity is found in the inter-fin region ($r/R \approx 0.67$), which is 95% of the absolute maximum velocity. Axial velocities vary in the angular direction in the inter-fin region but are almost independent of angle in the central core region. Steep velocity gradients are found in the vicinity of the solid boundary.

The existance of the second maximum velocity is due to the height of the fin. In the present work, the second maximum velocity is 5% less than the tube centerline velocity for $H = 0.667$. As $H > 0.667$, the second maximum velocity in the inter-fin region will increase. For $H = 1$, there will be only one maximum velocity. Conversely, if $H < 0.667$, the second maximum velocity will decrease and eventually vanish for very short fins.

Ornatskii et al [14] measured the mean velocity distribution along the symmetry axis of the finned tube segment channels (two rectangular interconnected channels). Their largest inter-fin region parameter b/ℓ for their air experiment corresponds approximately to the present geometry, but their velocity distributions show only a small dip at the fin tip radius. Velocity distributions similar to Figs. 16 & 17 have been predicted under fully developed laminar flow [8]. Soliman & Feingold [8] found that the closed loop isovels exist at $M = 6$, $H \geq 0.4$. According to Ivanovic [21], for the case of zero thickness fin, this closed loop isovels feature had not yet established in the fully developed turbulent for $M = 6$, $H = 0.45$.

Several investigators have tested the universality of the law of wall in non-circular ducts. It was generally found that the two empirical constants of the law of wall must be adjusted slightly to compensate for the nature of the wall surface and duct geometry.

The distributions of the axial mean velocity in terms u^+ and y^+ are shown in Figs. 19 and 20. The variables u^+ and y^+ are based on the local friction velocity. Table 2 lists the constants of the law of the wall as obtained using least-squares-fit for the various $y+$ ranges. The universal law of the wall based on 40 data points* is plotted in Fig. 19 for comparisons with selected experimental data (due to a small variation of y^+ in the angular direction) and the conventional universal law of the wall for smooth pipe. As shown in Fig. 19, the correlation of the present work is almost parallel to the law of the wall for smooth pipe.

Using the fin as the governing wall, the results at Re = 71,000 are shown in Fig. 20 which includes the conventional universal law of the wall for smooth flat plate [39]. The velocity distribution shows the following trend. In the y^* direction, u^+ increases with y^+ upto a certain y^* beyond which a reversal of trend occurs. The point of occurrence of reversal shifts to higher y^* with decreasing θ, i.e. toward the corner region. This feature may be caused by the presence of secondary flows. Also, it is not possible to make precise measurements of wall shear stress near the corner. As the corner is approached, the wall shear stresses ($0.6 \leq y^*/\ell < 1$) may actually fall more rapidly than those shown in Fig. 15. Alternatively, this may simply be one of the flow characteristics for a corner region.

5.7 Secondary Flow

The secondary flow results are shown in Figs. 21-24 inclusively. Regarding accuracy of the data, a rational assessment of the absolute accuracy was not possible, but as seen in Figs. 21-23, the data do exhibit a reasonable degree of consistence.

---

*See Figure 10: I = 10 to 13, J = 3 to 7; Re = 50,000 and 71,000.

Fig. 24 shows the resultant secondary velocity in a primary flow cell. The secondary flow is a double-cell counter-rotating pattern. An anti-clockwise rotating cell exists at $r/R = 0$ to 0.333. A clockwise rotating cell is found in the inter-fin region where r/R is greater than 0.333. The anti-clockwise secondary current transports the high momentum fluid from the tube centerline ($r/R = 0$) to the fin-tip-radius region ($r/R = 0.333$) via symmetry line ($\theta = 0$) and a return flow via symmetry line ($\theta = 30°$). A clockwise rotating secondary current transports the high momentum fluid into the corner and a return flow parallel to the fin before merging with the anti-clockwise rotating current for the upward deflection. This kind of double-cell counter-rotating pattern is also observed in the two-pin geometry of Kacker [30]. The strength of the clockwise rotating cell is much higher than the other cell, in which the maximum $\bar{V}$ and $\bar{W}$ are found. Maximum $\bar{W}$ had a magnitude of 3.1% of U_b in the downward flow near the tube wall, while maximum $\bar{V}$ had a magnitude of 4.6% of U_b in the return flow near the fin surface.

Though secondary velocities were large enough to be measured with the X-probe and slanting 45° probe, each method has a shortcoming. For the X-probe, error can be induced due to wire separation when operating in regions having large axial velocity gradients, i.e. near the solid boundary. Inaccuracy may arise in $\bar{V}$ near the fin surface and in $\bar{W}$ near the tube wall. The slanting 45° probe is not directly influenced by axial velocity gradients; however, the consecutive measurements of E_1 and E_2 were not necessarily obtained at the same location. In general, the 45° slanting probe results are probably more accurate near the solid boundary, whereas the X-probe results are preferable elsewhere.

5.8 Reynolds Normal Stresses

It is impractical to determine the accuracy of the Reynolds stresses measurements. However, based on repeatability (see Fig. 25), it is estimated that trend line accuracy for the normal stresses are within 10%. The results were consistent at the two Reynolds numbers; the results for Re = 71,000 are presented in Figs. 26 - 28 for ($\sqrt{\overline{u^2}}/\overline{u^*}$), ($\sqrt{\overline{v^2}}/\overline{u^*}$) and ($\sqrt{\overline{w^2}}/\overline{u^*}$) respectively. In these figures, the shape of the curves in the region where data is missing for $\theta = 10°$ (due to impractical measurements) is based on extrapolations from neighboring data.

Generally $\overline{u^2}$ is larger than $\overline{v^2}$ and $\overline{w^2}$ in duct flow. As shown in Figs. 26 - 28, the distributions of $\overline{u^2}$, $\overline{v^2}$ and $\overline{w^2}$ are similar. Because of the two orthogonal walls, $\overline{v^2}$ and $\overline{w^2}$ exhibit similar levels everywhere. All three normal stresses are almost equal in the core region; i.e. $r/R < 0.333$, and also in the inter-fin region where $r/R \approx 0.667$, $\theta = 25°$ and $30°$.

As seen in Figs. 26 - 28, normal stresses would start from high levels in the vicinity of the wall (high turbulence production zone)and decrease leaving the wall. This decrease would continue upto a location where the effect of two orthogonal walls would neutralize each other. Thereafter the normal stresses would increase. A peak would be expected above and/or near the fin tip. Thereafter the normal stresses would decrease gradually to the tube centerline. The normal stresses distributions display two noticeable features. Firstly, the peaks appear accentuated. Secondly, whereas the peaks start out opposite the fin tip for $\theta = 10°$, it progressively shifts with increasing θ to $r/R \approx 0.25$ at $\theta = 30°$. This phenomenon can be explained by secondary flow; this is the region where the two cells have merged after passing over the fin tip and fin flank surface. The upward current of the anti-clockwise secondary flow which returns to the tube centerline tides away the highly turbulent fluid from the centerline and shifts the peak towards its flow direction. On the contrary, the upward current of the clockwise secondary flow exerts little effects because its turbulence is weakened in the widening flow area.

5.9 Turbulent Kinetic Energy

From the contour plot of turbulent kinetic energy in Fig. 29, one can easily recognize the same secondary flow pattern; but it is more pronounced. In the inter-fin region, there is a very strong effect of secondary flow motion towards the corner region. This secondary flow causes the turbulent kinetic energy contour to bulge towards the corner region. Due to the weak strength of the secondary flow in the central core region, the bulging pattern is not as noticeable as that due to the clockwise cell of secondary flow in the inter-fin region.

5.10 Reynolds Shear Stresses

Figs. 30 and 31 shows the radial distributions of normalized Reynolds stresses ($\overline{uv}/(\overline{u^*})^2$, $\overline{uw}/(\overline{u^*})^2$) as obtained using the X-probe technique. The normalized Reynolds stress distributions corresponding to Re = 50,000 and 71,000 were not a single distribution. Also, the Reynolds stress results did not always repeat at either Reynolds number. Hence, the present results are not reliable and the distribution of eddy viscosity could not be determined.

The local average values of the combined results (based on four sets of Reynolds stress measurements) are shown in Figs. 32 - 39 to show the general trend of the radial distribution.

Attempts in measuring Reynolds stresses was unsuccessful. The causes could not be explained. In spite of the inaccurate measurements, the radial distributions shown in Fig. 30 reflect the dependence of $\overline{uv}$ on the axial mean velocity gradient $\partial\overline{U}/\partial r$, i.e., $\overline{uv}$ is generally negative in sign whenever $\partial\overline{U}/\partial r$ is negative and vice versa. The $\overline{uv}$ distributions also appear to have angular dependence in that the negative swings in $\overline{uv}$ become less pronounced with decreasing θ. As shown in Fig. 31, the sign of $\overline{uw}$ remains negative throughout the primary flow cell for Re = 71,000. For Re = 50,000 (Figs. 36-39) the occassional positive value was measured in the core region and near the tube wall.

The magnitudes of $\overline{uv}/(\overline{u^*})^2$ ranged from about -0.55 to +0.50 while $\overline{uw}/(\overline{u^*})^2$ ranged from about -0.1 to -0.9 for Re = 71,000 whereas extreme average values (Figs. 36-39) were in the range +0.2 to -1.0 for the two Reynolds number.

6.0 CONCLUDING REMARKS

The experimental study of fully developed turbulent flow through an internally finned tube has revealed the following:

1) The experimental isothermal friction factors are 5% - 8% higher than those predicted by the Prandtl-Nikuradse correlation.

2) The average of the wall shear stresses on the tube wall is almost the same as the average on the fin flank surface.

3) Double peak velocity occurs along the 30° symmetry line; absolute maximum velocity is at the tube centerline. Closed looped isovels are found in the inter-fin region.

4) There are two counter-rotating cells of secondary flow within each of twelve primary flow cells. The maximum secondary velocity is about 4½% of the bulk axial velocity.

5) The turbulent kinetic energy field shows more significant influence by the secondary flow than the mean axial velocity field and wall shear stress distribution, especially near the corner region.

The present work indicates that secondary flows, which are presumably in turn affected by fin height, have an important influence on the flow structure. It is therefore suggested that the turbulence measurements should be conducted for internally finned tubes with different fin heights. Since attempts at measuring Reynolds shear stresses were unsuccessful, further investigation should be done for H = 0.667. Also, an investigation might be conducted on the influence of two adjacent walls upon the flow structure in the corner region.

7.0 ACKNOWLEDGEMENTS

The author would like to acknowledge the patience and guidance extended to him by Dr. A.C. Trupp. He expresses his gratitude to his fellow students in the Department of Mechanical Engineering and particularly to Nady Said and Shriek Burhanuddin, for their assistance. The funding provided by Natural Sciences and Engineering Research Council Canada for this research is gratefully acknowledged.

8.0 REFERENCES

1. Vasilchenko, Y.A. and Barbaritskaya, M.S., "Resistance with Nonisothermal Fluid Flow in Tubes with Longitudinal Fins", Thermal Engineering, Vol. 16, No. 1, 1969, pp. 28-35.

2. Vasilchenko, Y.A. and Barbaritskaya, M.S., "Heat Transfer in Tubes with Longitudinal Fins", Thermal Engineering, Vol. 16, No. 5, 1969, pp. 105-109.

3. Watkinson, A.P., Miletti, D.L., and Kubanek, "Heat Transfer and Pressure Drop of Internally Finned Tubes in Laminar Oil Flow", ALCHE-ASME Heat Transfer Conference, San Francisco, Calif., August, 1975, ASME Paper No. 75-HT-41.

4. Soliman, H.M. and Feingold, A., "Heat Transfer Pressure Drop and Performance Evaluation of a Quintuplex Internally Finned Tube", ASME Paper No. 77-HT-46, 1977.

5. Marner, W.J. and Bergles, A.E., "Augmentation of Tubeside Laminar Flow Heat Transfer by Means of Twisted-Tape Inserts, Static-Mixer Inserts and Internally Finned Tubes", Sixth International Heat Transfer Conference, Toronto, Canada, Aug. 7-11, 1978, Vol. 2, pp. 583-588.

6. Hu, M.H. and Chang, Y.P., "Optimization of Finned Tubes for Heat Transfer in Laminar Flow", Journal of Heat Transfer, Vol. 95, 1973, pp. 332-339.

7. Masliyah, J.H. and Nandakumar, K., "Heat Transfer in Internally Finned Tubes", Journal of Heat Transfer, Vol. 96, 1976, pp. 257-261.

8. Soliman, H.M. and Feingold, A., "Analysis of Fully Developed Laminar Flow in Longitudinal Internally Finned Tubes", The Chemical Engineering Journal, Vol. 14, 1977.

9. Soliman, H.M. and Feingold, A., "Analysis of Heat Transfer in Internally Finned Tubes under Laminar Flow Conditions", Proc. Sixth International Heat Transfer Conference, Toronto, Canada, Aug. 7-11, 1978, Vol. 2, pp. 571-576.

10. Soliman, H.M., "The Effect of Fin Material on Laminar Heat Transfer Characteristics of Internally Finned Tubes", The 18th National Heat Transfer Conference, San Diego, Calif., Aug. 6-8, 1979, pp. 95-102.

11. Brouillette, E.C., Miffin, T.R., and Myers, J.E., "Heat Transfer and Pressure Drop Characteristics of Internal Finned Tubes", ASME Annual Meeting, New York, Dec., 1957, ASME Paper No. 57-A-47.

12. Hilding, W.E. and Coogan, C.H., "Heat Transfer and Pressure Loss Measurements in Internally Finned Tubes", Seventh National Heat Transfer Conference, Cleveland, August, 1964, ASME Symposium on Air-Cooled Heat Exchanges, pp. 57-85.

13. Lipets, A.U., Zholudov, Ya. S., Antonov, A. Ya, and Gramov,G.V., "The Temperature Regime and Hydraulic Resistance of Tubes with Internal Longitudinal Fins", Heat Transfer - Soviet Research, Vol. 1, No. 5, Sept. 1969, pp. 86-94.

14. Ornatskii, A.P., Shcherbakov, V.P., and Semena, M.G., "Investigation of Velocity Distribution in Tubes with Internal Longitudinal Fins", Thermal Engineering, Vol. 17, No. 2, 1970, pp. 108-111.

15. Bergles, A.E., Brown, G.S., and Snider, W.D., "Heat Transfer Performance of Internally Finned Tubes", Eleventh National Heat Transfer Conference, Tulsa, Aug. 1971, ASME Paper No. 71-HT-31.

16. Watkinson, A.P., Miletti, D.L., and Tarassoff, P., "Turbulent Heat Transfer and Pressure Drop in Internally Finned Tubes", ALCHE Symposium Series, Vol. 69, No. 131, 1973, pp. 94-103.

17. Watkinson, A.P., Miletti, D.L. and Kubonek, G.R., "Heat Transfer and Pressure Drop of Internally Finned Tubes in Turbulent Air Flow", ASHRAE Trans., Vol. 81, Part 1, 1975, pp. 330-349.

18. Russell, J.J., and Carnavos, T.C., "Air Cooling of Internally Finned Tubes", CEP, Feb., 1977, pp. 84-88.

19. Carnavos, T.C., "Cooling Air in Turbulent Flow with Internally Finned Tubes", Seventh National Heat Transfer Conference, Salt Lake City, Aug. 1977, AICHE Paper No. 4.

20. Carnavos, T.C., "Heat Transfer Performance of Internally Finned Tubes in Turbulent Flow", National Heat Transfer Conference, San Diego, Calif., Aug. 1979.

21. Ivanovic, M., "Prediction of Flow and Heat Transfer in Internally Finned Tubes", Ph.D. Thesis, University of Minnesota, July, 1977.

22. Minchenko, F.P., and Shvartsman, G.S., "Heat Transfer Enhancement in Finned Steam-generating Tubes", Heat Transfer - Soviet Research, Vol. 11, No. 2, 1979, pp. 14-23.

23. Gee, D.L., and Webb, R.L., "Forced Convection Heat Transfer in Helically Rib-roughened Tubes", International Journal Heat Mass Transfer, Vol. 23, 1980, pp. 1127-1136.

24. Royal, J.H., and Bergles, A.E., "Augmentation of Horizontal In-Tube Condensation by Means of Twisted-Tape Inserts and Internally Finned Tubes", Journal of Heat Transfer, Vol. 100, 1978, pp. 17-24.

25. Hoagland, L.C., "Fully Developed Turbulent Flow in Straight Rectangular Ducts - Secondary Flow, Its Causes and Effect on the Primary Flow", D.Sc. Thesis, Massachusette of Technology, 1960.

26. Leutheusser, H.J., "Turbulent Flow in Rectangular Ducts", Journal of the Hydraulic Division, ASCE, Vol. 89, No. HT3, May 1963, pp. 1-19.

27. Brundrett, E., and Baines, W.D., "The Production and Diffusion of Vorticity in Duct Flow", Journal of Fluid Mechanics, Vol. 19, 1964, pp. 375-394.

28. Gessner, F.B., and Jones, J.B., "On Some Aspects of Fully Developed Turbulent Flow in Rectangular Channels", Journal of Fluid Mechanics, Vol. 23, Part 4, 1965, pp. 689-713.

29. Launder, B.E., and Ying, W.M., "Secondary Flows in Ducts of Square Cross-section", Journal of Fluid Mechanics, Vol. 54, Part 2, 1972, pp. 289-295.

30. Kacker, S.C., "Some Aspects of Fully Developed Turbulent Flow in Non-circular Ducts", Journal of Fluid Mechanics, Vol. 57, Part 3, 1973.

31. Lyall, H.G., "Measurement of Flow Distribution and Secondary Flow in Ducts Composed of Two Square Interconnected Sub-Channels", A Symposium on Internal Flow, University of Salford, April 20-22, 1971, Paper No. 33, pp. E16-E23.

32. Aly, A.M.M., Trupp, A.C., and Gerrand, A.D., "Measurements and Prediction of Fully Developed Turbulent Flow in a Triangular Duct", Journal of Fluid Mechanics, Vol. 85, Part 1, 1978, pp. 57-83.

33. Zamir, M. and Young, A.D., "Experimental Investigation of the Boundary Layer in a Streamwise Corner", The Aeronautical Quarterly, Nov. 1970, pp. 313-339.

34. Gerrard, A.D., "Turbulent Flow in an Equilateral Triangular Duct", M.Sc. Thesis, University of Manitoba, 1976.

35. Lawn, C.J., "Turbulence Measurements with Hot-Wire at B.N.L.", Central Elec. Gen. Board, Berkley Nuclear Labs. Rep. RD/B/M 1277, April 1969.

36. Patel, V.C., "Calibration of the Preston Tube and Limitations on its Use in Pressure Gradients", Journal of Fluid Mechanics, Vol. 23, Part 1, 1965, pp. 185-208.

37. Ower, E., and Pankhurst, R.C., <u>The Measurement of Air Flow</u>, 4th ed., Pergamon, Oxford, 1966.

38. Walls, J.A.B., "The Correction of Hot-Wire Readings for Proximity to a Solid Boundary", Journal of Fluid Mechanics, Vol. 12, 1962, pp. 388-396.

39. Hinze, J.O., <u>Turbulence</u>, 2nd ed., McGraw-Hill, New York, 1979.

APPENDIX

CORRECTIONS AND ERROR ANALYSIS

Corrections for various types of errors were investigated for both the Pitot tube and hot-wire probe. The displacement of effective center of Pitot tube corrections suggested by Ower & Panhurst [37] were used in the local axial mean velocity measurements. This correction was almost negligible in the present work.

All Pitot tube measurements were made using a Betz projection manometer which had an accuracy of $\pm$ 0.05 mm water. The uncertainty in the experimental results could be calculated by

$$\frac{dU}{U} = \frac{1}{2}\frac{dh}{h}$$

where

dU/U = uncertainty for axial mean velocity measurements, %

dh = accuracy of the manometer, mm water

h = velocity head, mm water.

The following table summarized the range of uncertainty in Pitot tube measurements.

Re	Velocity head (mm water)		Uncertainty (%)	
	max	min	max. vel. head	min.vel.head
50,000	31.4	15.3	.08	.16
71,000	62.6	31.15	.04	.08

Assuming a blend of systematic errors and random errors, it is safe to consider that the Pitot tube data is accurate to within 1%.

Due to the uncertainty of the turbulence effect correction, no corrections were made to velocity measurement via the hot-wire probe. Also, this correction becomes important only in the vicinity of a solid boundary.

When using a hot-wire probe for velocity measurements close to a solid boundary, it may be necessary to correct hot-wire readings due to heat conduction through the fluid to the wall. Walls [38] suggested that the wall effect correction should be expected to apply only within the viscous sublayer. In the present work, the last grid point was in the turbulent core region always ($y^+ \geq\sim 100$ for fin and $y^+ \geq\sim 300$ for tube wall); therefore, no correction was required for the data.

The measurements of normal stresses ($\overline{u^2}$, $\overline{v^2}$ and $\overline{w^2}$) and Reynolds stresses ($\overline{uv}$ and $\overline{uw}$) were corrected for tangential cooling effects as suggested by Lawn [35]. For the DISA hot-wire probes, the k was taken as 0.23. Due to the complexity of the signal processing circuit as shown in Fig. 9, the absolute accuracy of the data was not known.

For the X-wire probe technique, the measurements of Reynolds shear stresses are more susceptible than normal stresses because each of the former involves multiplying two signals (V'_{1+2} and V'_{1-2}) together and then time-averaging, whereas the latter depends only on one time-average signal. When the signals are of approximately the same order of magnitude, the combined error of Reynolds shear stresses may be larger than that of normal stresses.

Table 1: Turbulent Entrance Lengths for Various Types of Ducts

		L/D_h	
		With B.L. Tripping	Without B.L. Tripping
Circular pipe			< 49
Square duct	Gessner & Jones [28]	40	
Rectangular duct	Gessner & Jones [28]	60	
Square duct	Ying & Launder [29]		69
Equilateral triangular duct	Gerrard [34]		133
Finned tube segment channel[1]	Ornatskii [14]		30 - 40
Finned tube segment channel[2]	Ornatskii [14]		30 - 33

[1] $0.09 \leq b/\ell \leq 1.2$

[2] $0.25 \leq b/\ell \leq 1.9$

Table 2: Empirical Constants for the Law of the Wall

	A	B	Deviation %	y^+ range
Wall (N = 20)	7.05	2.04	2.96	289-647
Wall (N = 30)	2.16	2.85	2.88	289-973
Wall (N=40)	3.61	2.62	3.02	289-1352
Fin (N=32)	4.39	2.59	3.08	107-864
Fin (N=48)	6.17	2.27	4.23	107-1213
Fin (N=64)	8.73	1.84	5.03	197-1568

Deviation = $[\frac{1}{N} \Sigma (u^+_{exp} - u^+_{cor})^2]^{\frac{1}{2}}/u^+_{exp,\ av.}$

N = No. of data points

1. DUCT
2. NOZZLE
3. CANVAS COUPLINGS
4. DAMPER
5. FAN SECTION
6. SILENCER
7. DIFFUSER
8. CORNER WITH TURNING VANE
9. DIFFUSER
10. CORNER WITH TURNING VANE
11. TRANSITION
12. SCREEN SECTION
13. CONTRACTION CONE
14. NOZZLE
15. TEST SECTION A
16. TEST SECTION B

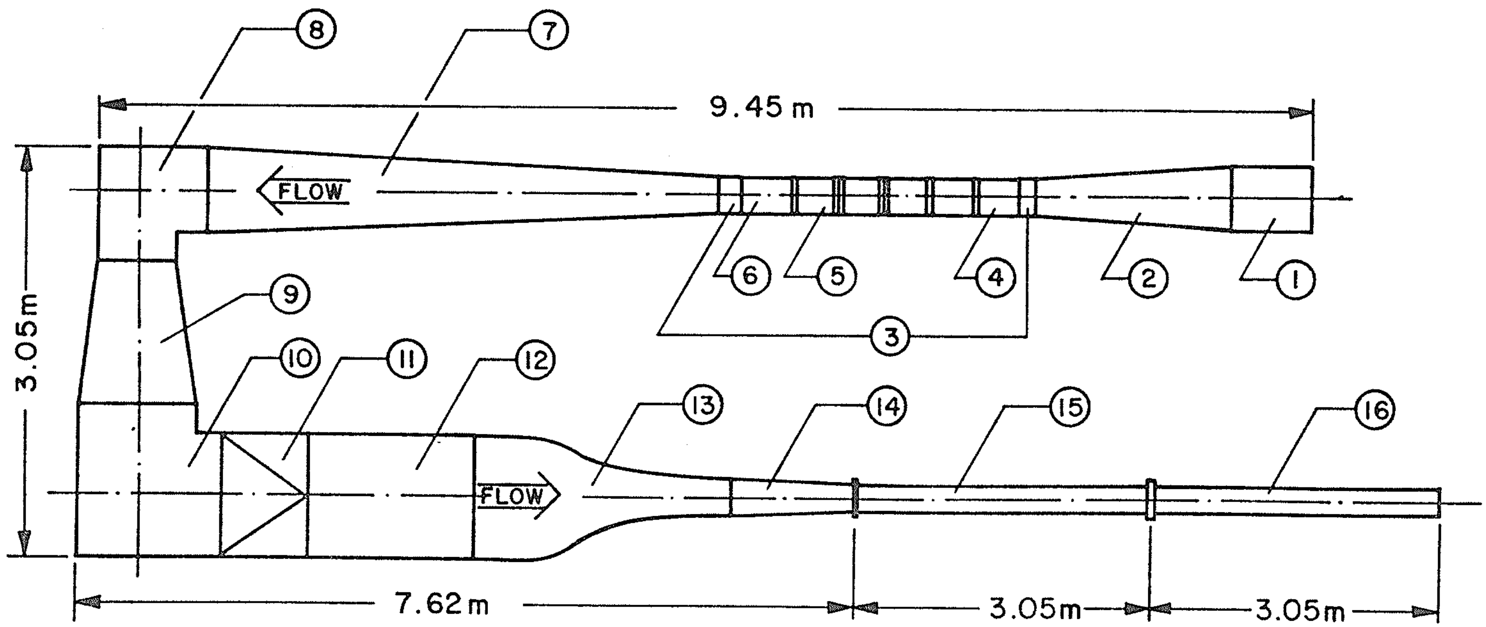

Figure 1: Wind Tunnel Layout.

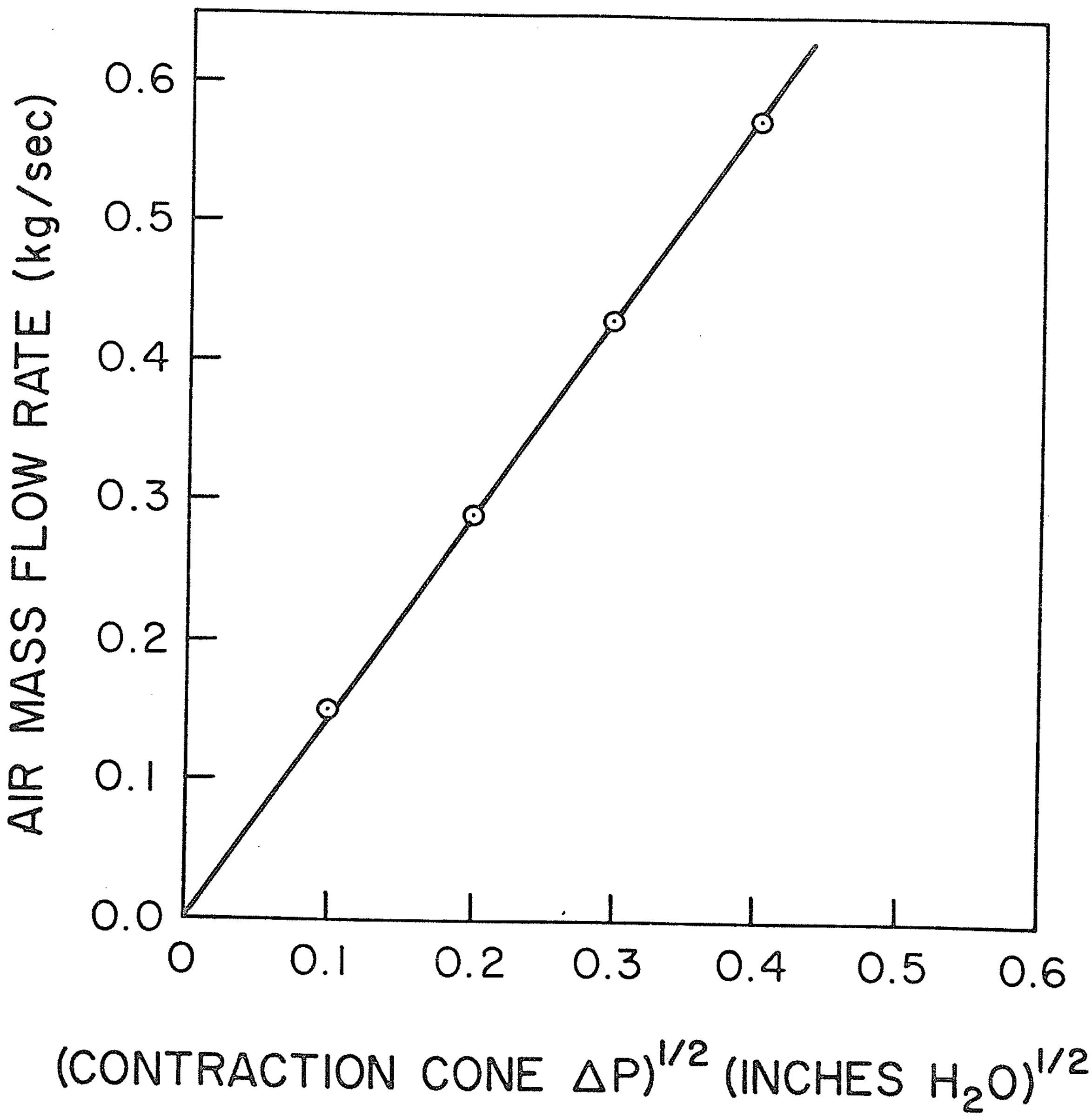

Figure 2: Wind Tunnel Calibration.

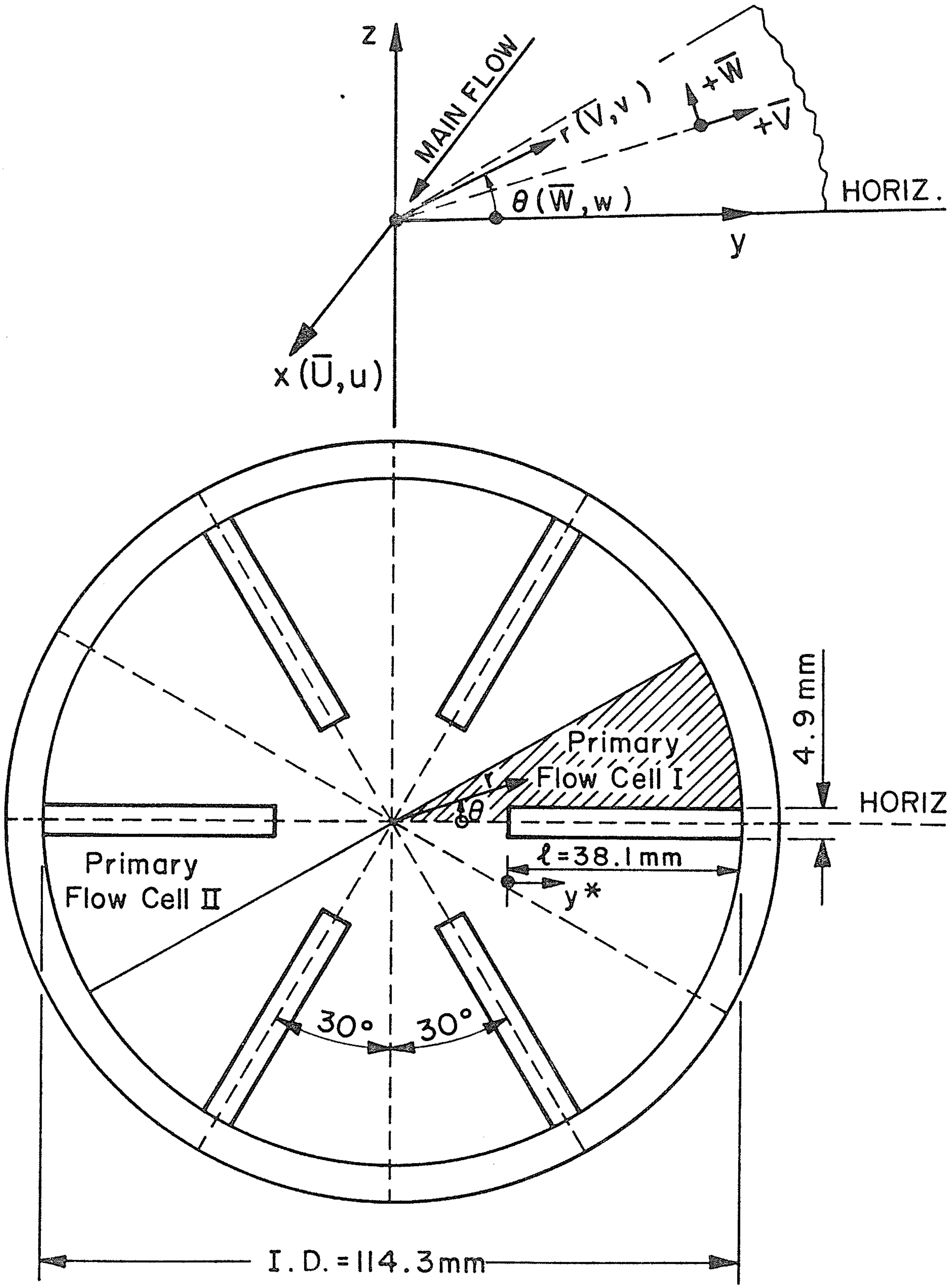

Figure 3: Cross-section of Internally Finned Tube Test Section.

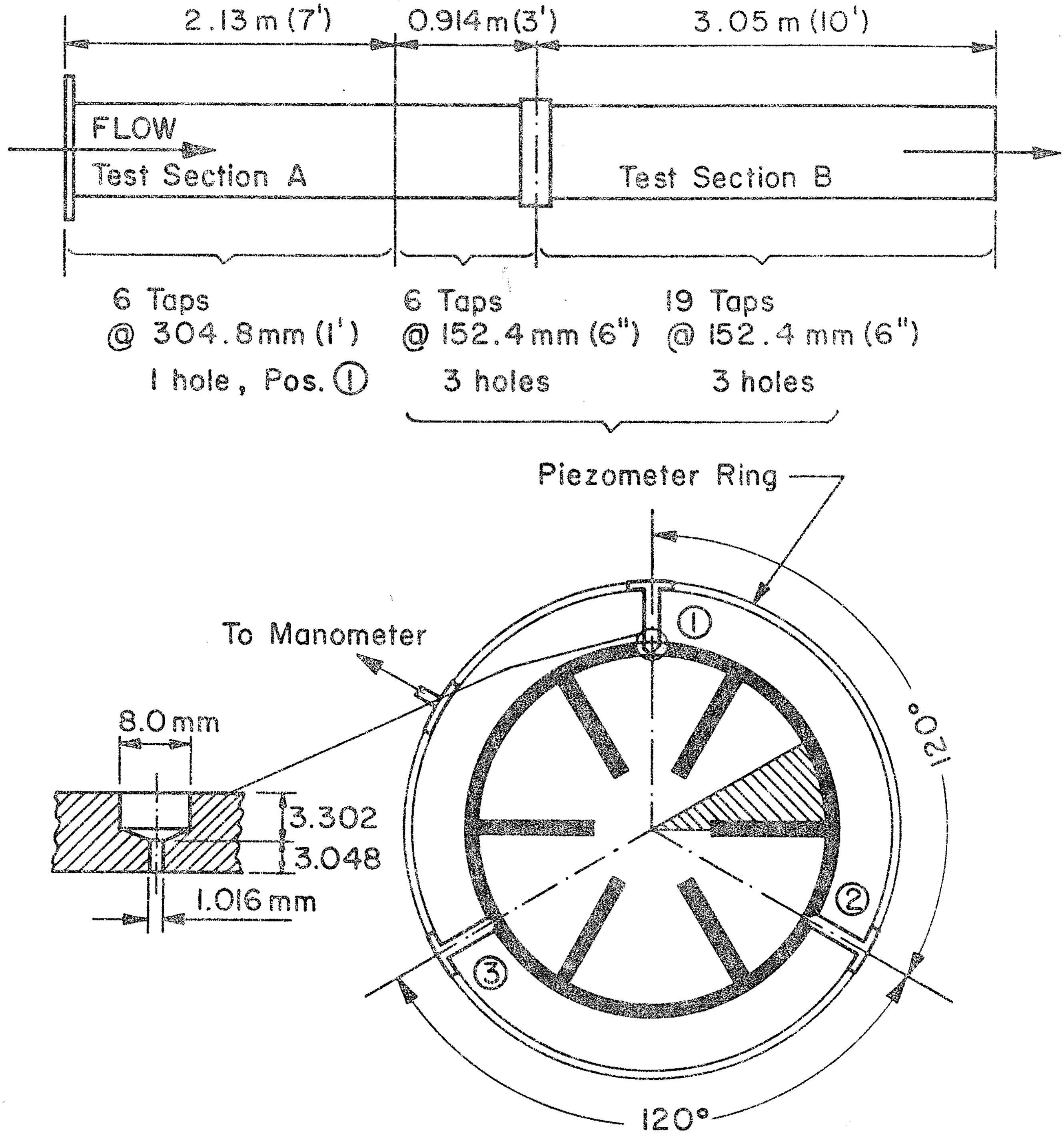

Figure 4: Test Section

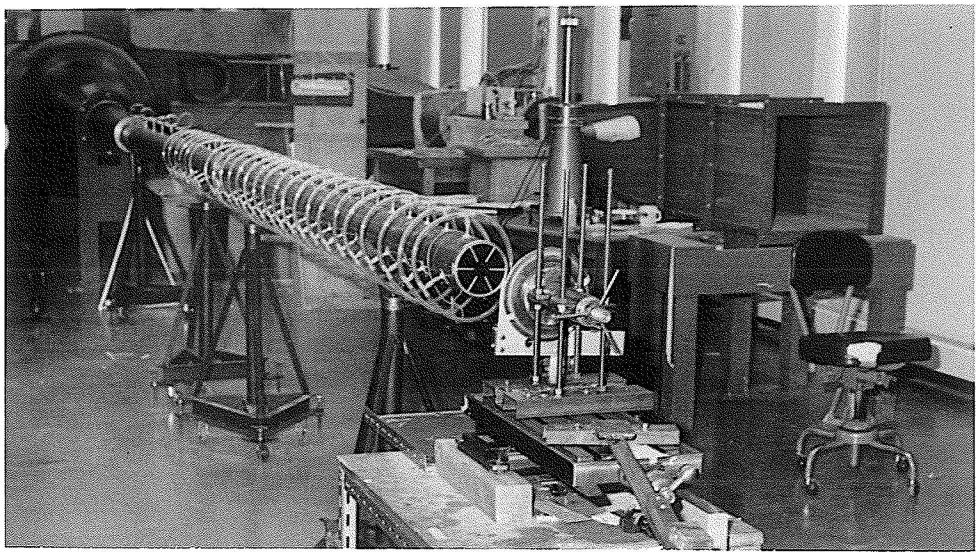

Figure 5: Internally Finned Tube Test Facility.

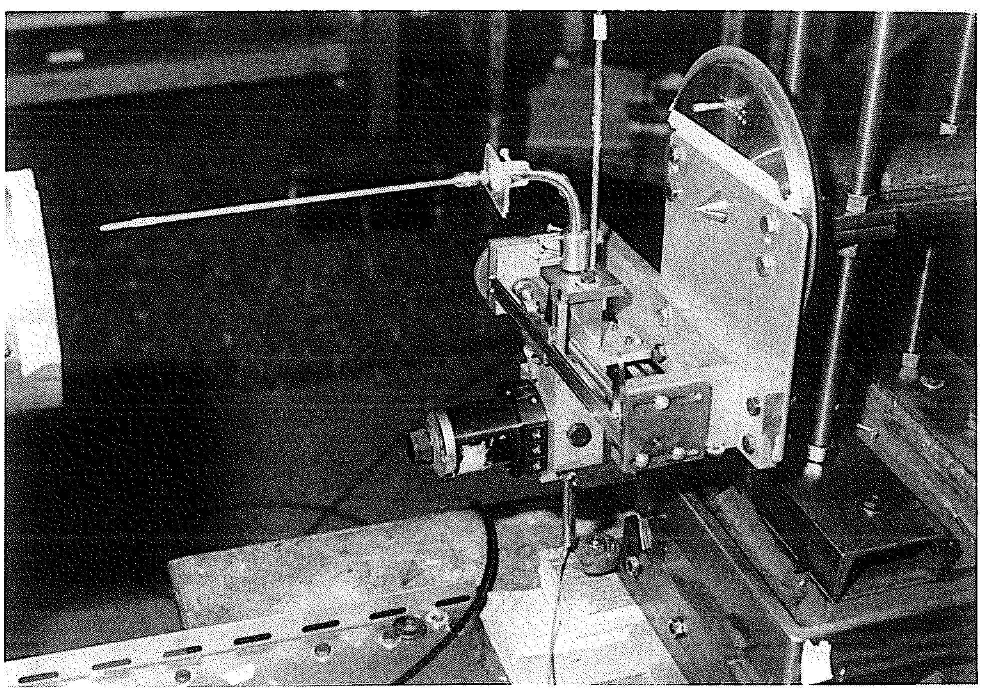

Figure 6: Traversing Mechanism.

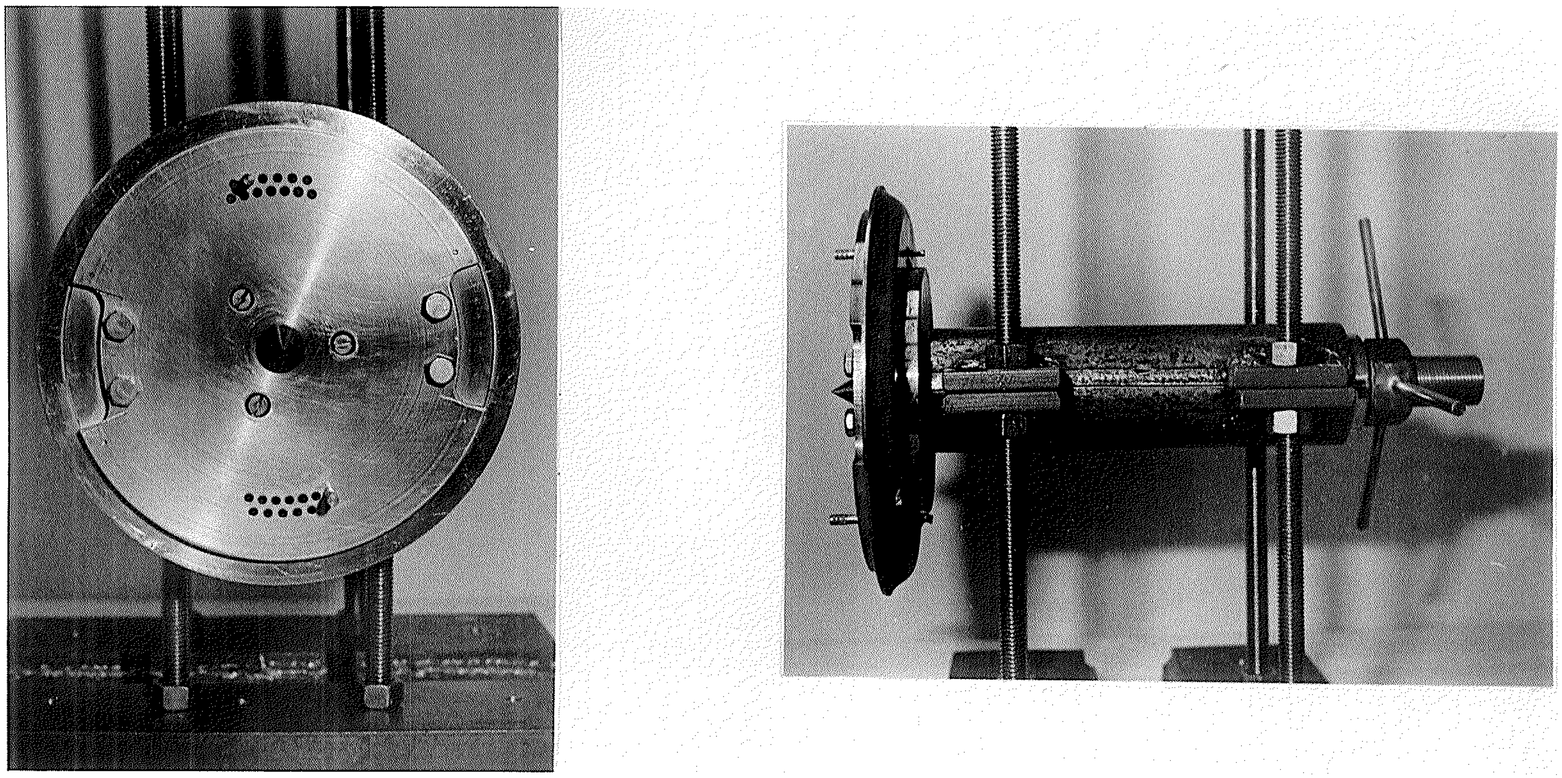

(a) (b)

Figure 7: θ-direction Traversing Mechanism.

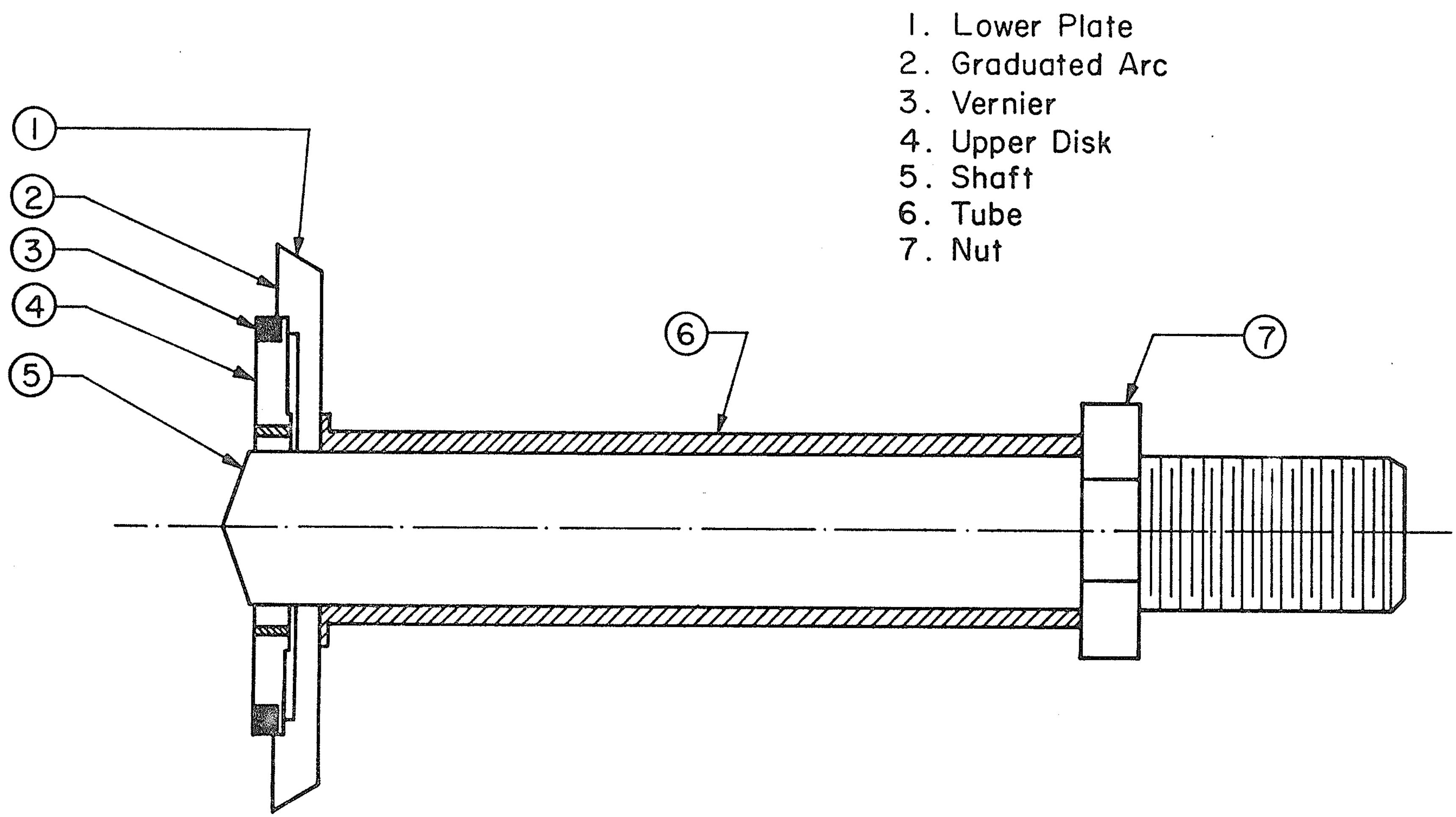

Figure 8: Sectional Drawing of the θ-direction Traversing Mechanism.

AC

$$A = V_1' = C_1\left[u + v(1-k^2)/(1+k^2)\right]$$

$$B = V_2' = C_2\left[u - v(1-k^2)/(1+k^2)\right]$$

FOR $C_1 = C_2 = C$:

$$A + B = V_{1+2}' = 2Cu$$

$$A - B = V_{1-2}' = 2Cv(1-k^2)/(1+k^2)$$

$$(A+B)(A-B) = V_{1+2}' \cdot V_{1-2}' = 4C^2 uv(1-k^2)/(1+k^2)$$

DC

$$A = E_1 = C_1\left[\bar{U} + \bar{V}(1-k^2)/(1+k^2)\right]$$

$$B = E_2 = C_2\left[\bar{U} - \bar{V}(1-k^2)/(1+k^2)\right]$$

FOR $C = C_1 = C_2 = E_{\text{¢}} / \bar{U}_{\text{¢}}$:

$$(A+B)(A-B) = A^2 - B^2$$

$$4C^2\bar{U}\bar{V}(1-k^2)/(1+k^2) = E_1^2 - E_2^2 .$$

$$V = \frac{\bar{U}_{\text{¢}}^2}{\bar{U}}\left(\frac{1+k^2}{1-k^2}\right)\left[\frac{E_1^2 - E_2^2}{(2E_{\text{¢}})^2}\right]$$

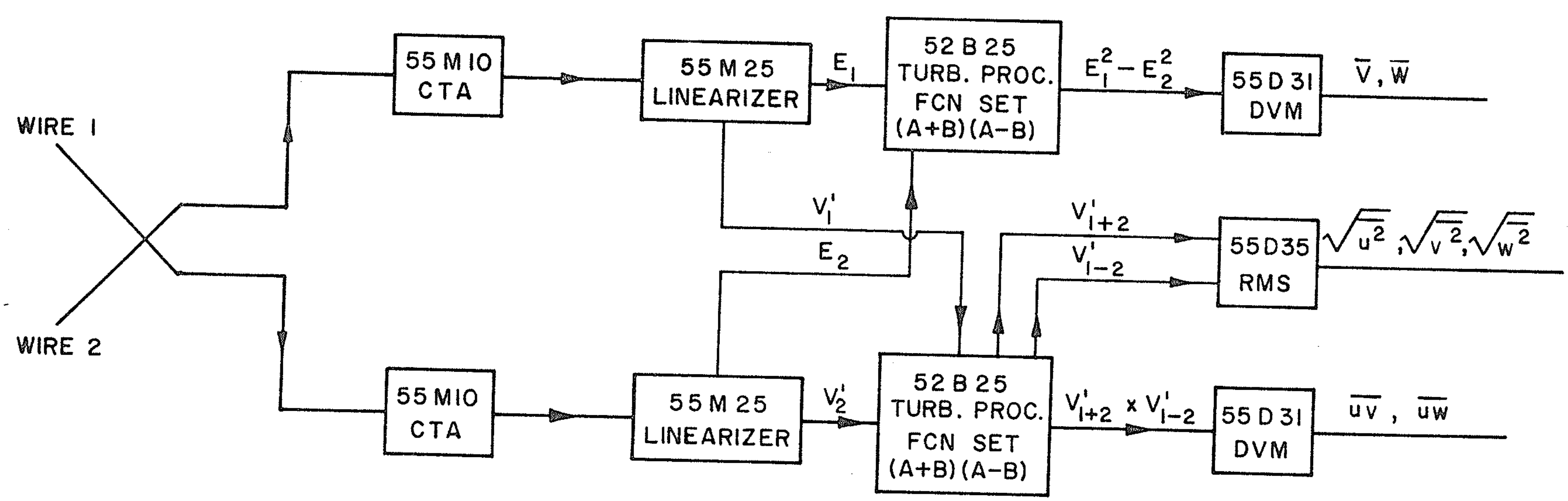

Figure 9: Signal Processing Circuit.

I	r/R
1	0.0
2	0.088
3	0.178
4	0.244
5	0.333
6	0.411
7	0.489
8	0.567
9	0.644
10	0.722
11	0.800
12	0.867
13	0.911
14	1.0

J	θ (Deg.)
1	0
2	5
3	10
4	15
5	20
6	25
7	30

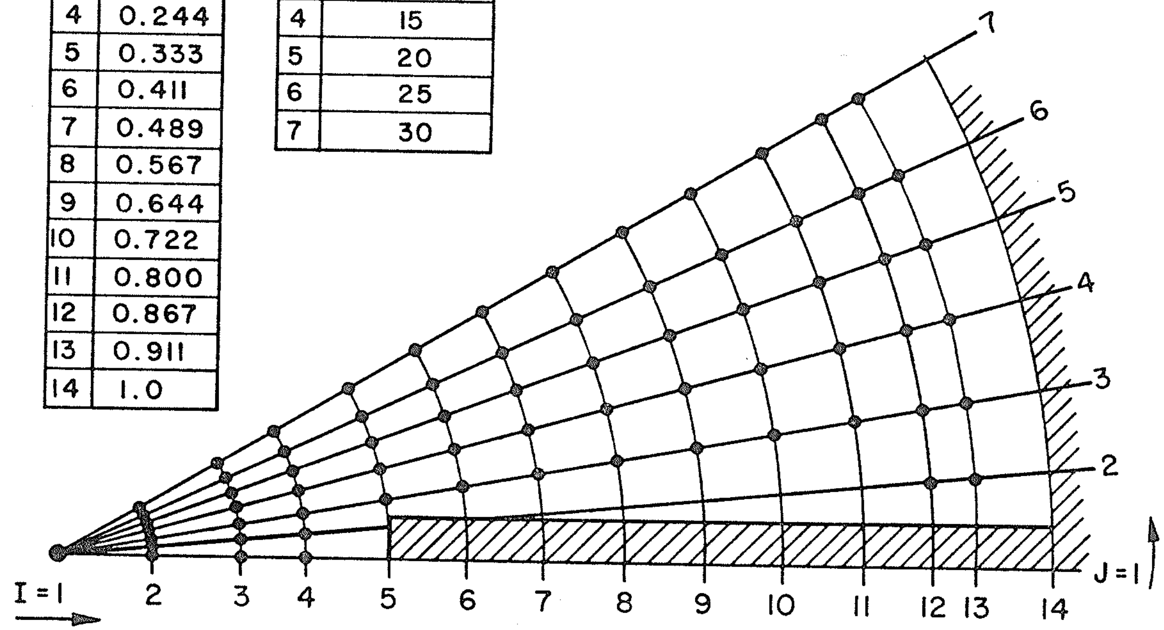

Figure 10: Primary Flow Cell Grid Points.

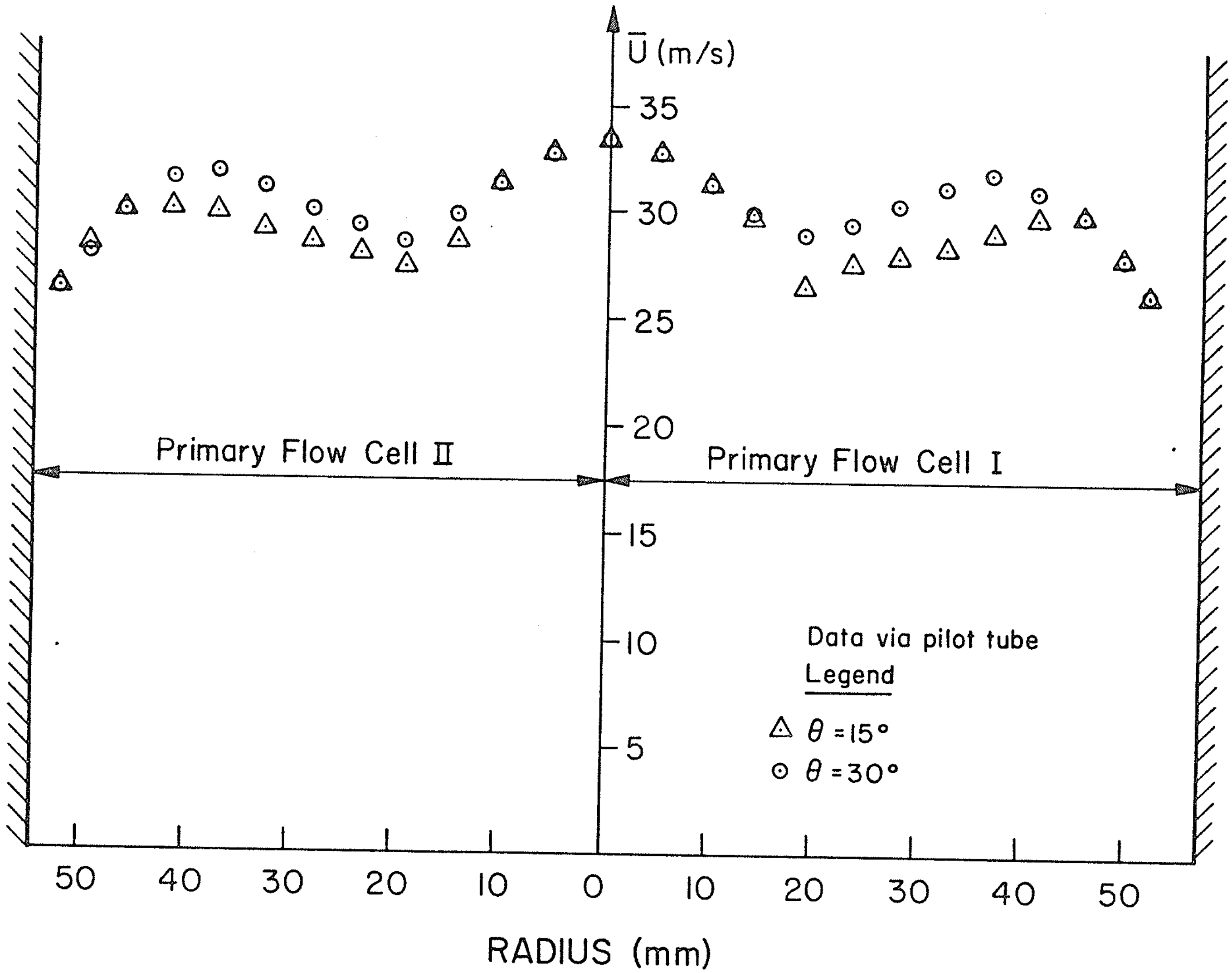

Figure 11: Radial Distributions of $\bar{U}$ in Primary Flow Cell I & II, Re = 71,000.

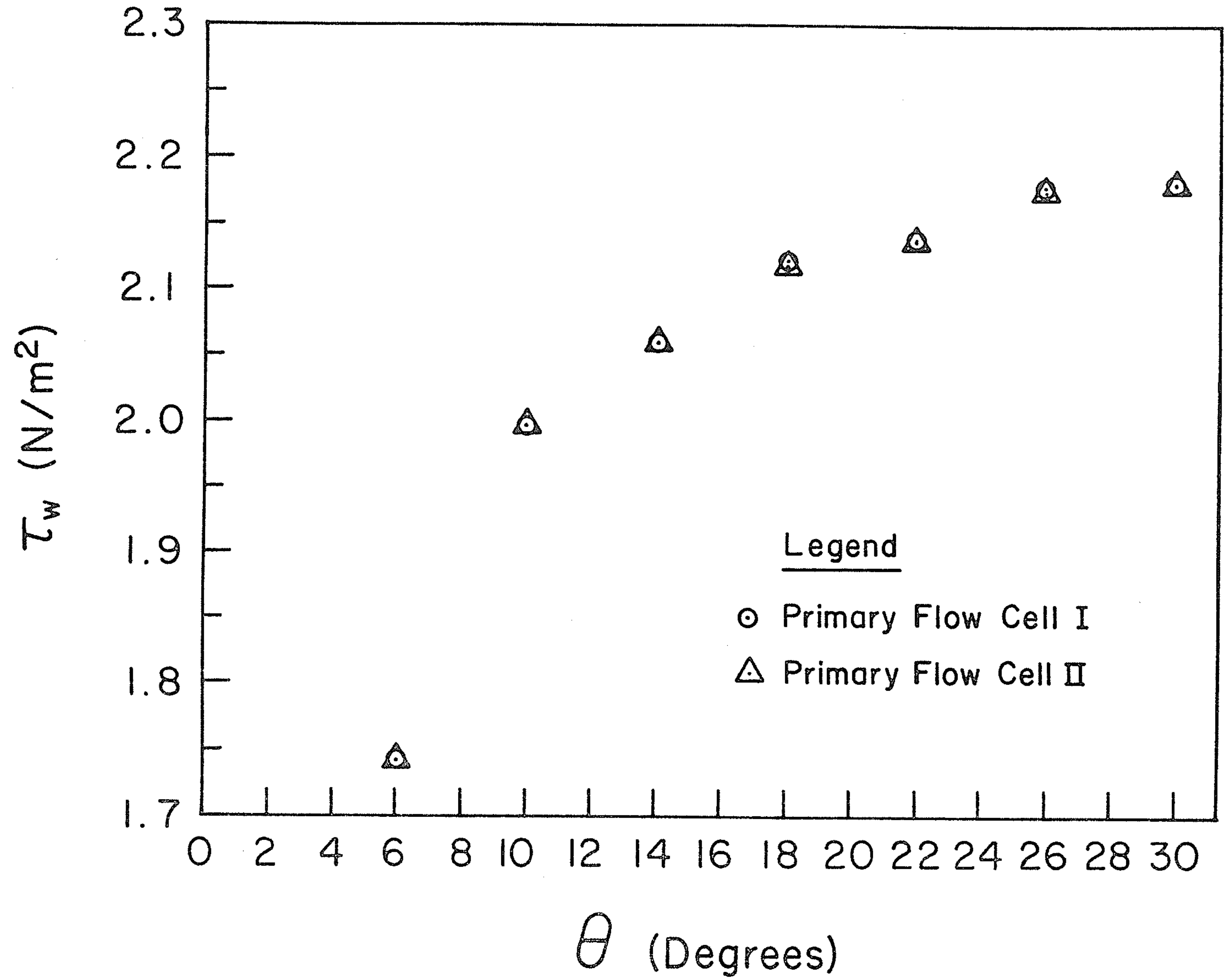

Figure 12: Local Wall Shear Stress Distributions in Primary Flow Cell I & II Along the Tube Wall, Re = 71,000.

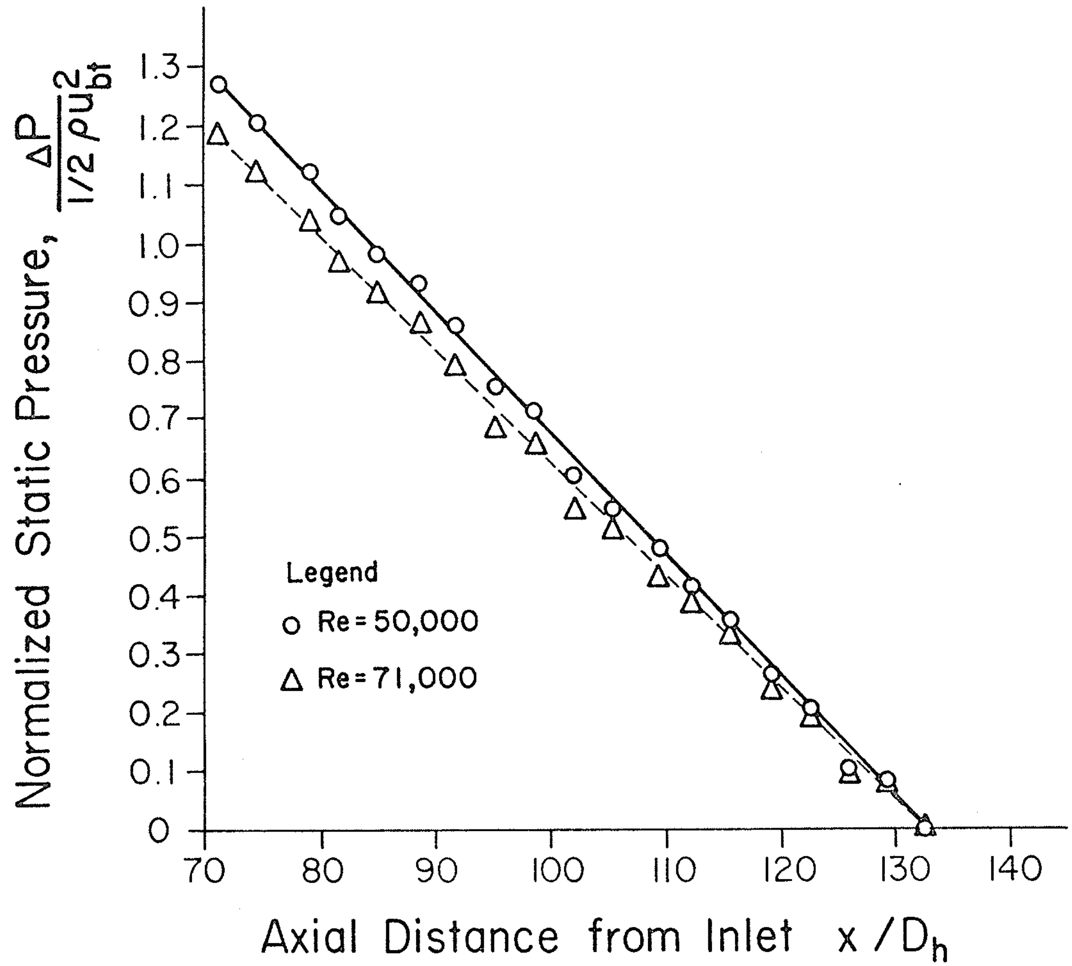

Figure 13: Axial Static Pressure Distribution.

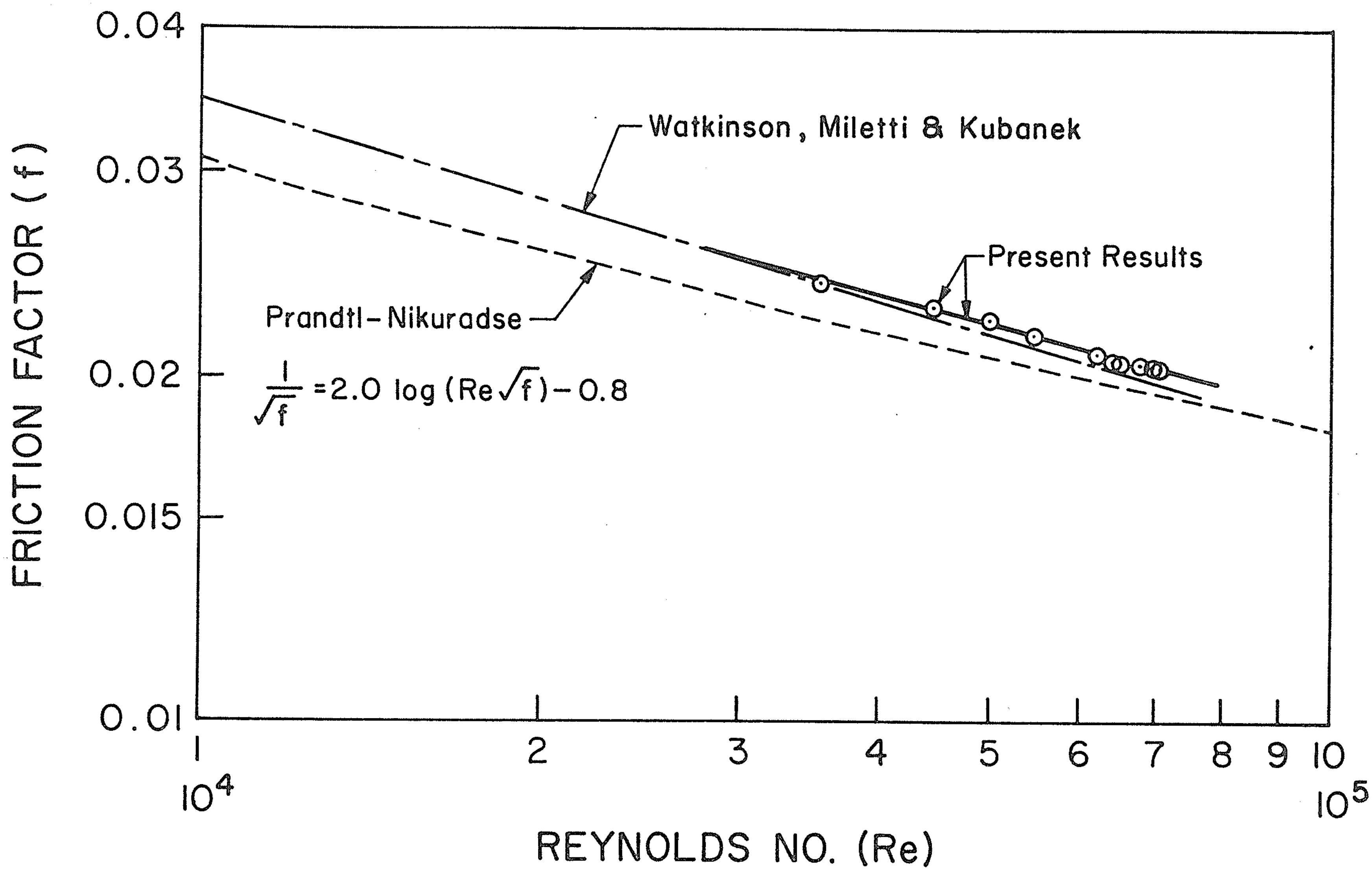

Figure 14: Friction Factor vs Reynolds Number for the Internally Finned Tube.

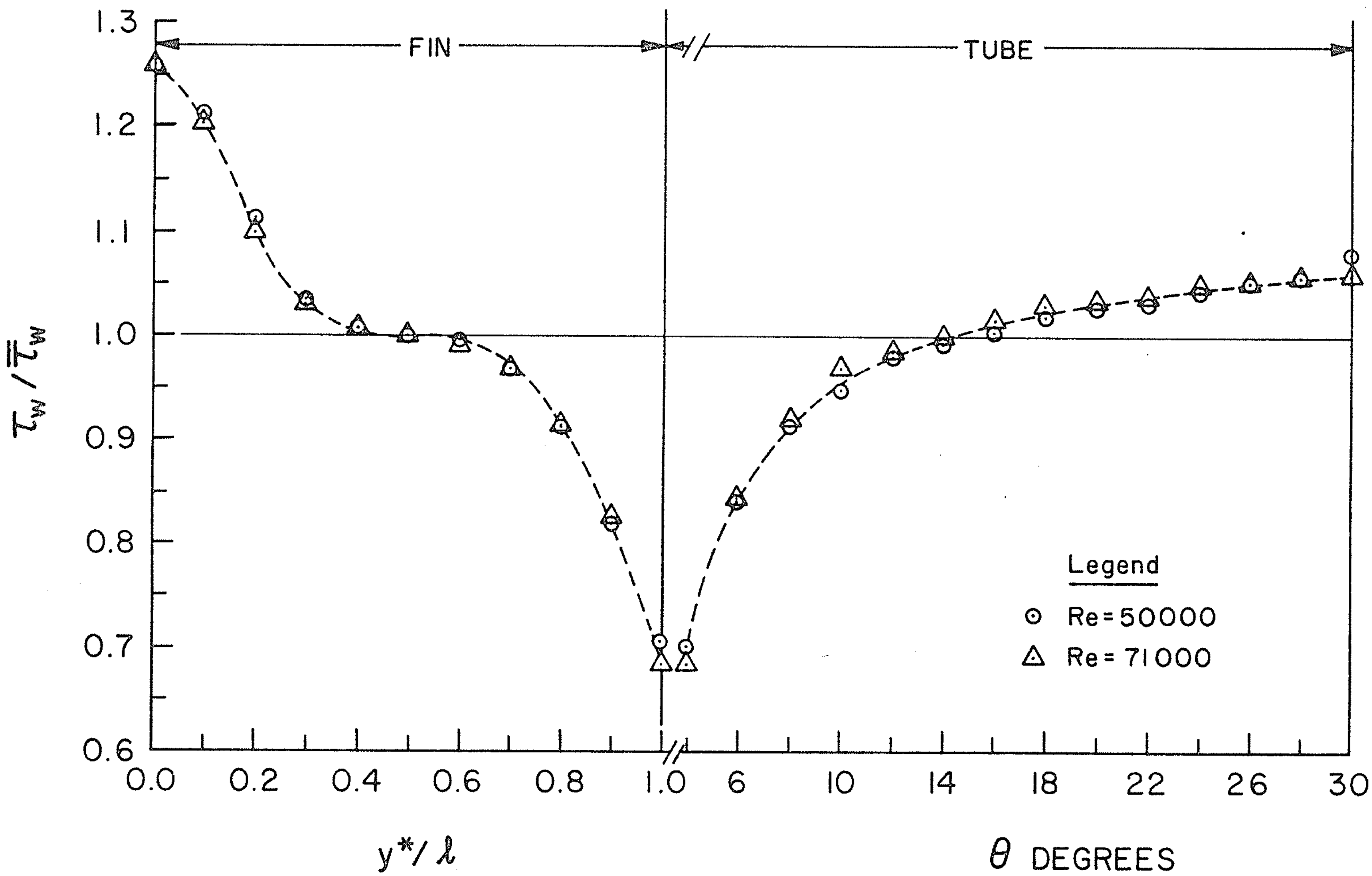

Figure 15: Local Wall Shear Stress Distributions.

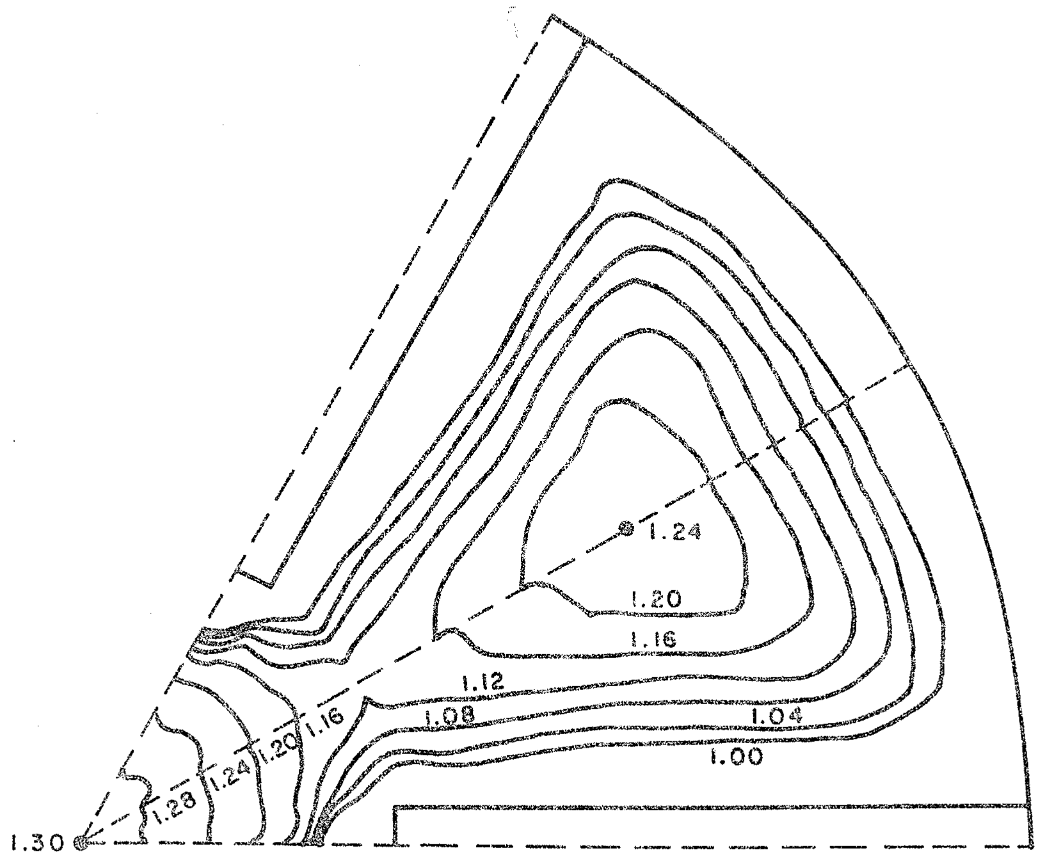

Figure 16: Isovels of U/U_b, Re = 50,000;Top-Hot Wire, Bottom-Pitot Tube.

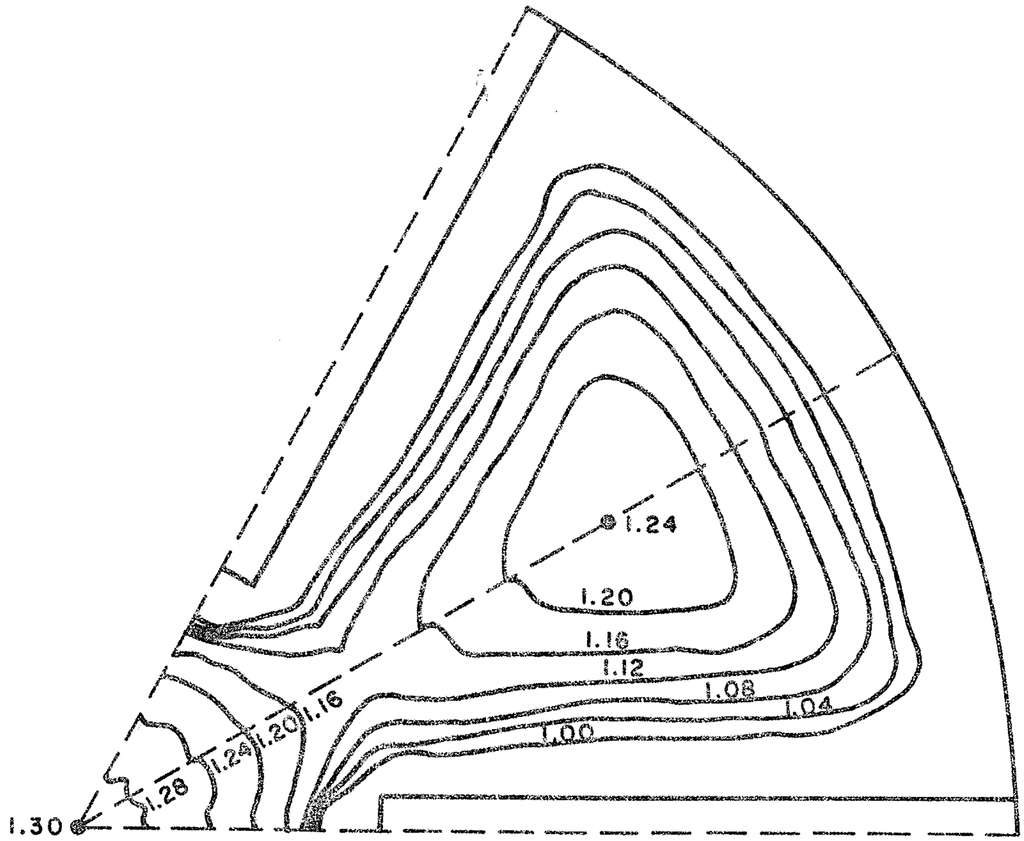

Figure 17: Isovels of U/U_b, Re = 71,000;Top-Hot Wire, Bottom-Pitot Tube.

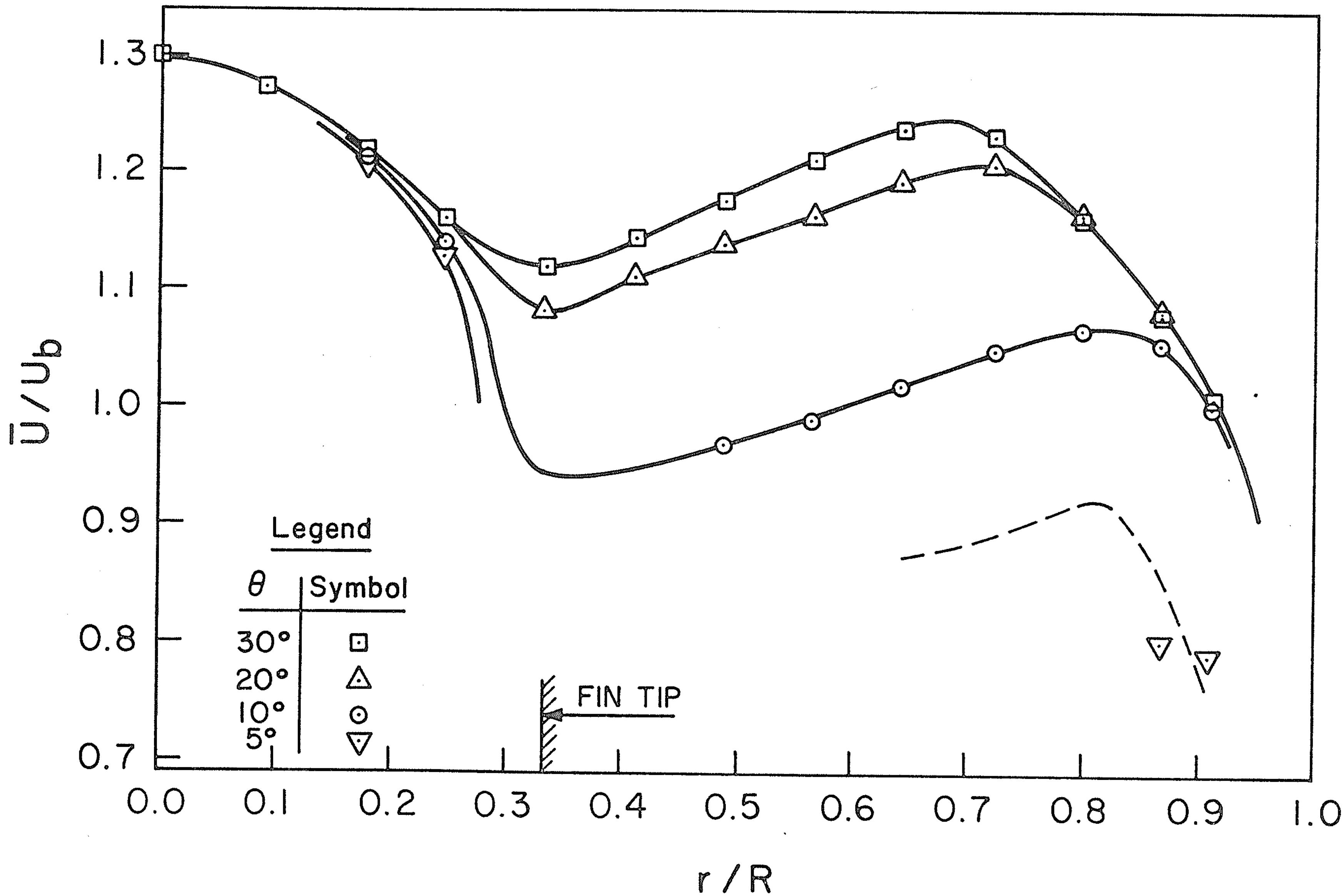

Figure 18: Radial Distributions of $\bar{U}/U_b$ in Primary Flow Cell, Re = 71,000.

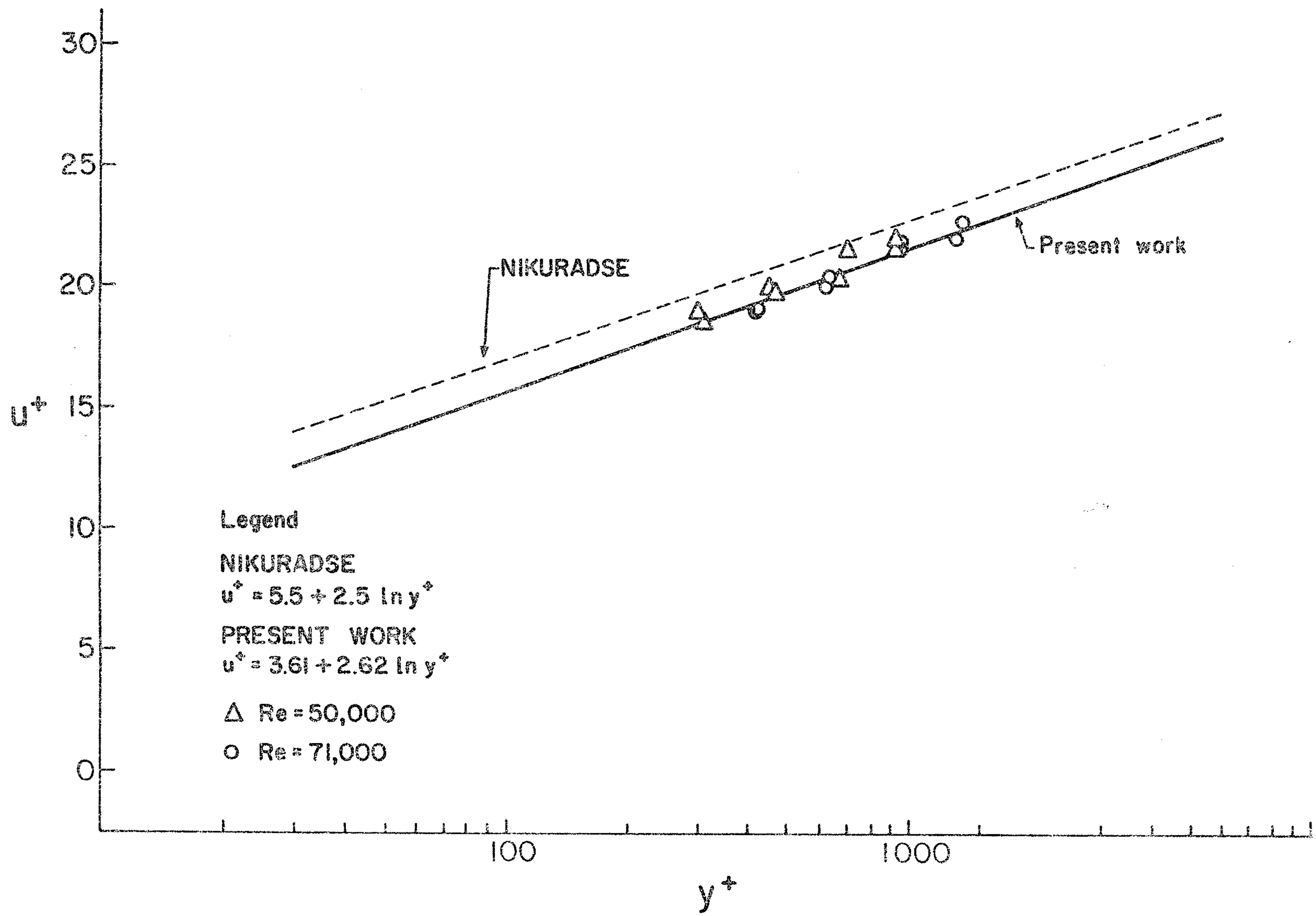

Figure 19: u^+ Versus y^+ (Tube).

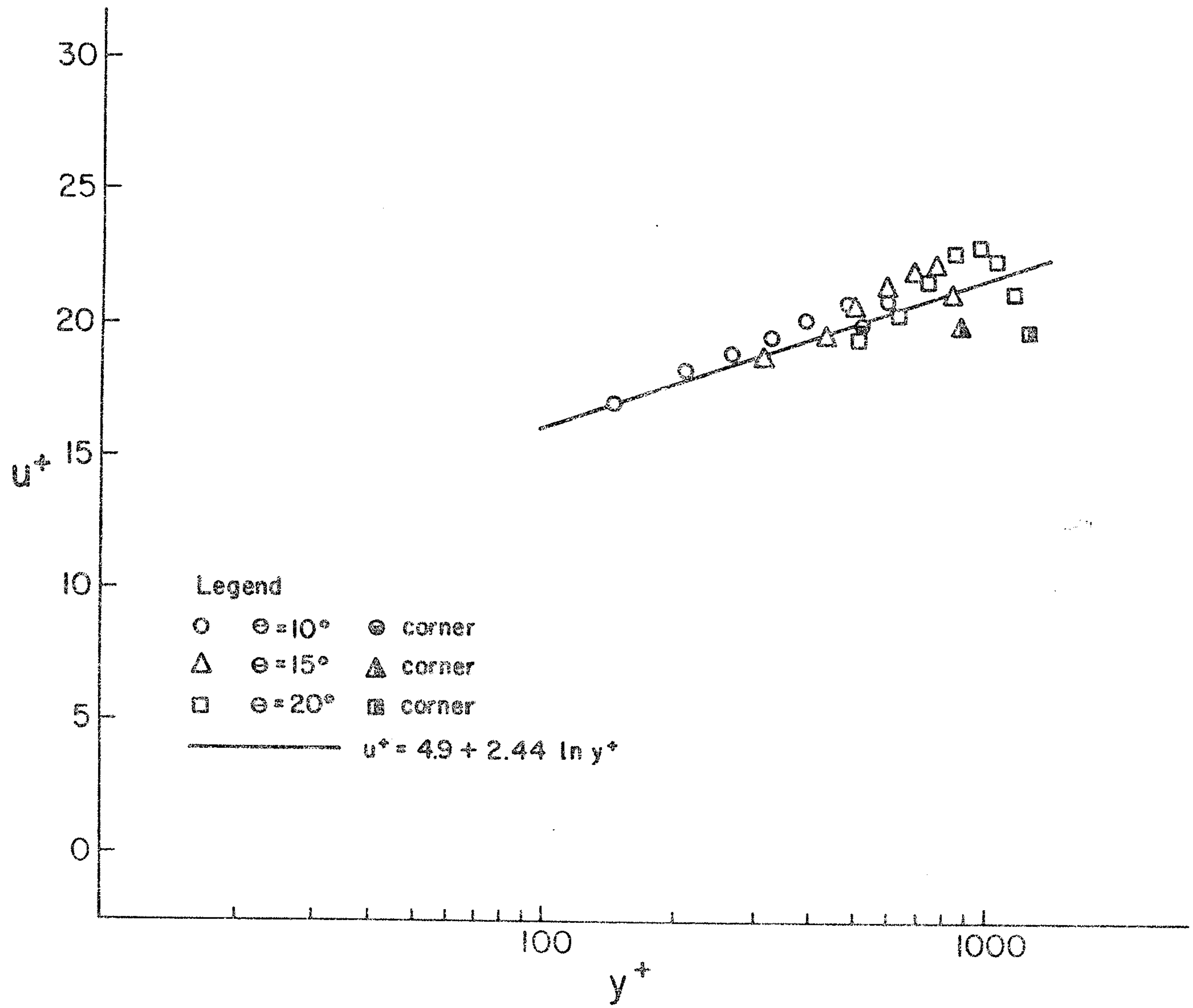

Figure 20: u^+ Versus y^+ (Fin), Re = 71,000.

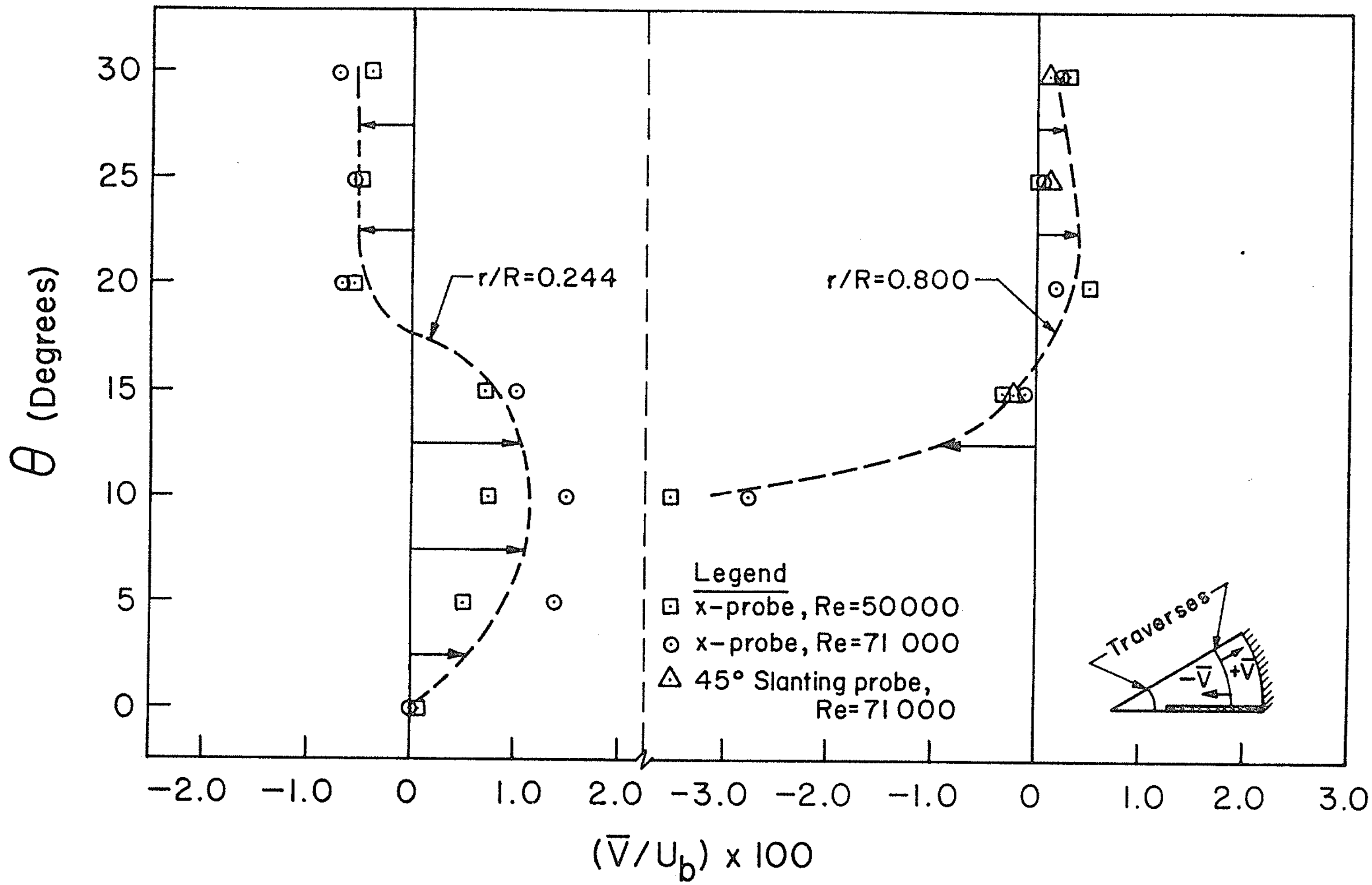

Figure 21: Circumferential Distributions of $\bar{V}$.

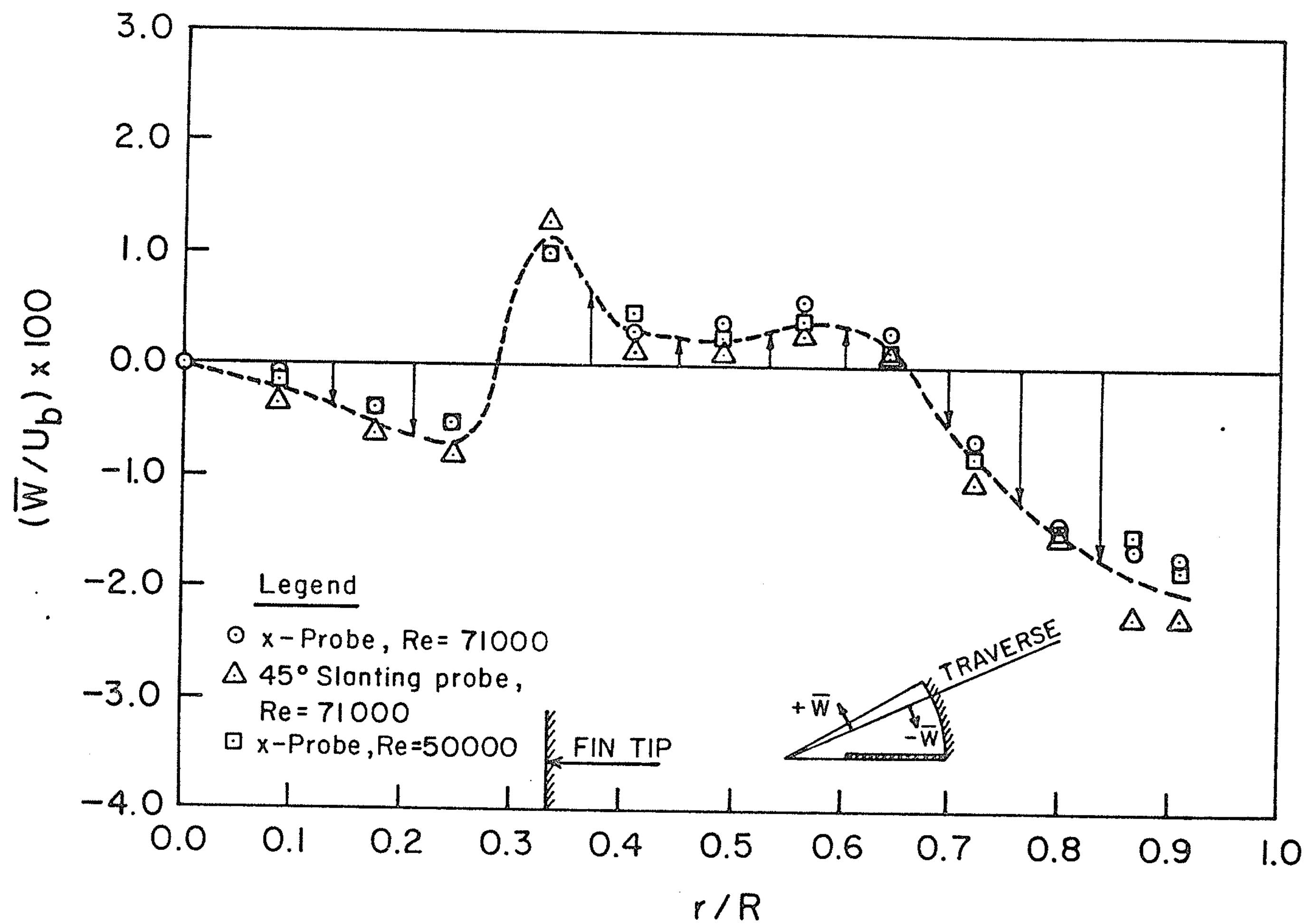

Figure 22: Radial Distributions of $\bar{W}$ at θ = 25°.

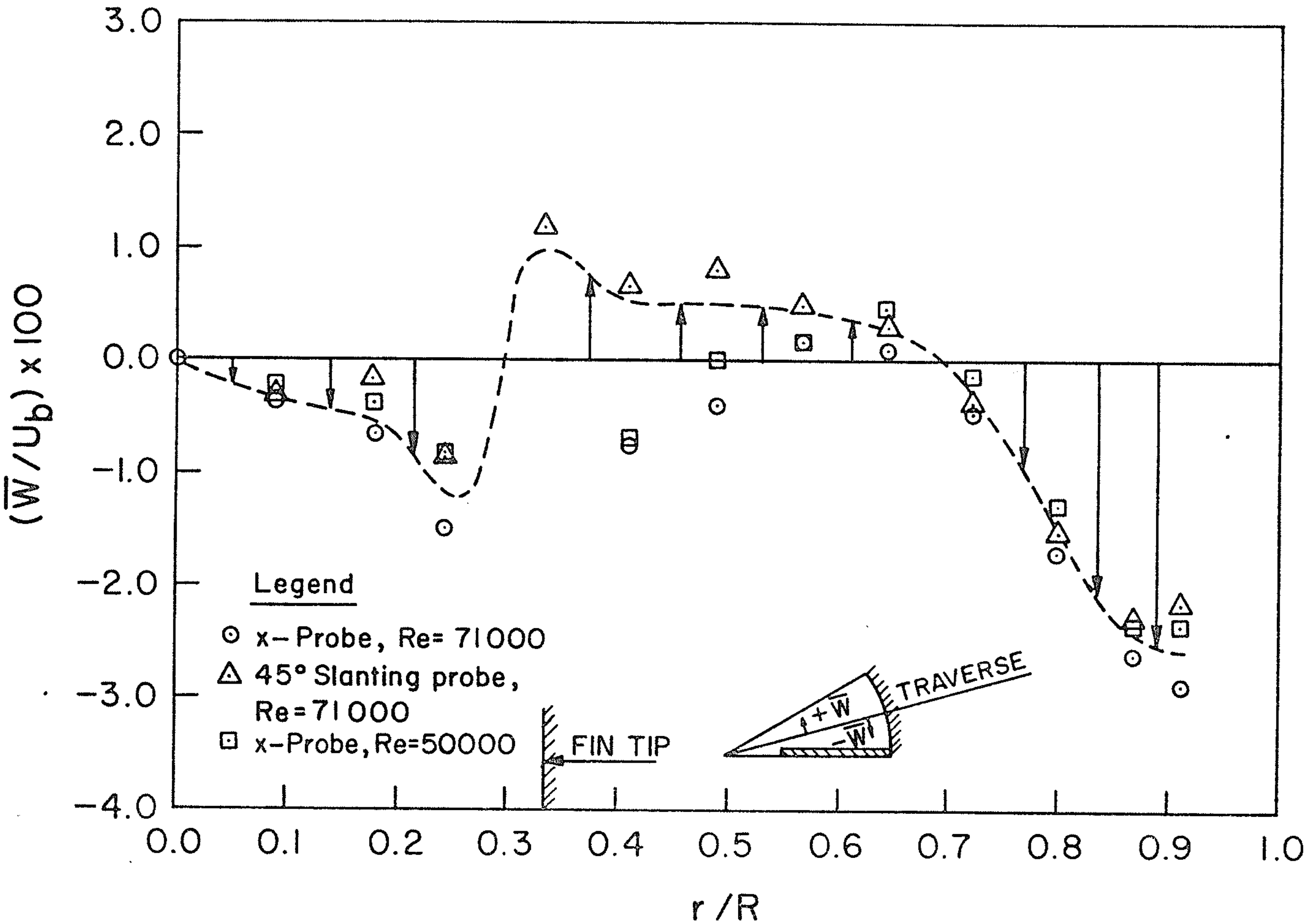

Figure 23: Radial Distributions of $\overline{W}$ at θ = 15°.

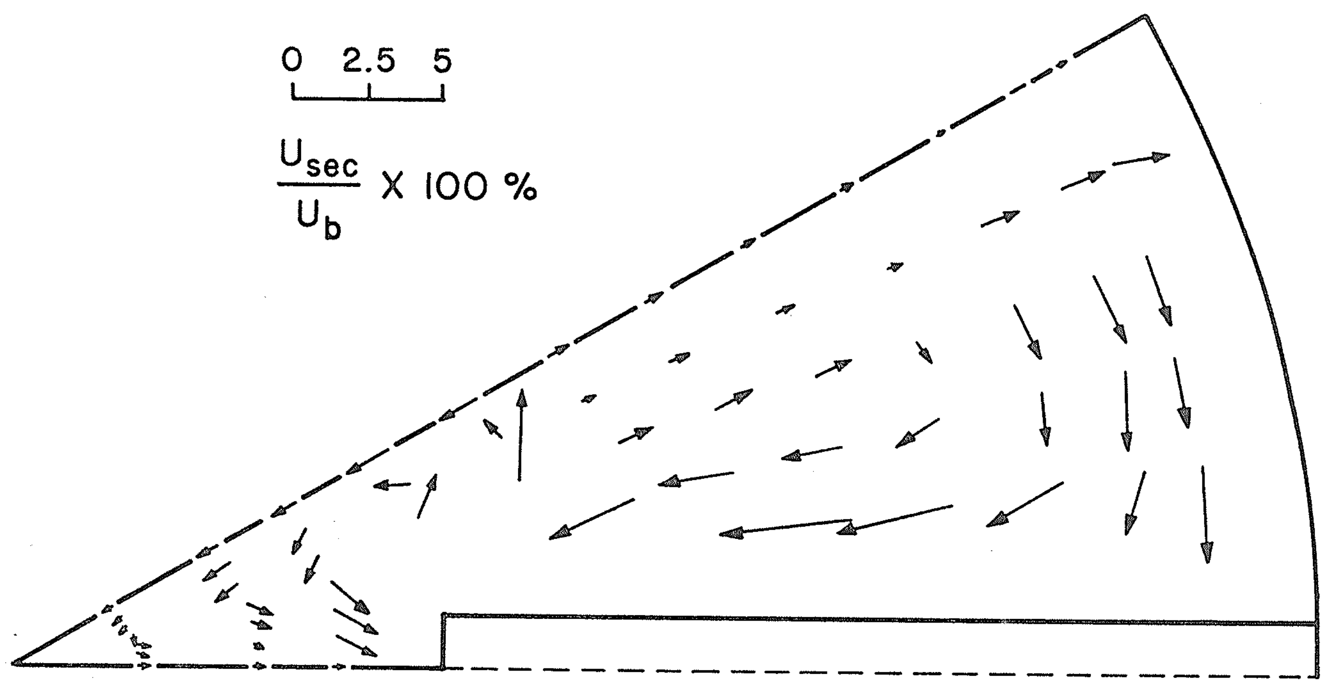

Figure 24: Secondary Flow in the Primary Flow Cell, Re = 71,000.

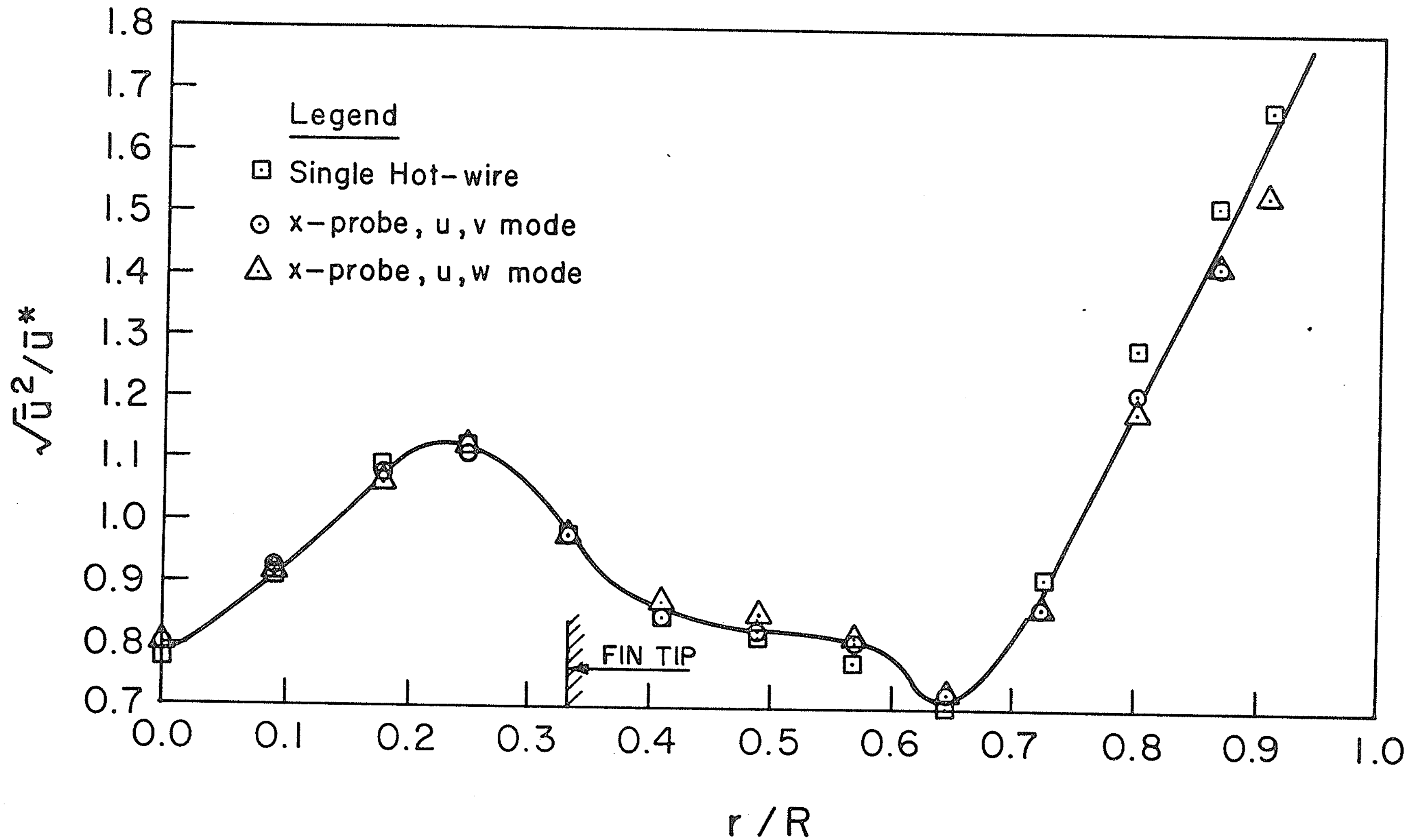

Figure 25: Radial Distribution of $\sqrt{\bar{u}^2}$ Along Symmetry Line (θ = 30°), Re = 71,000.

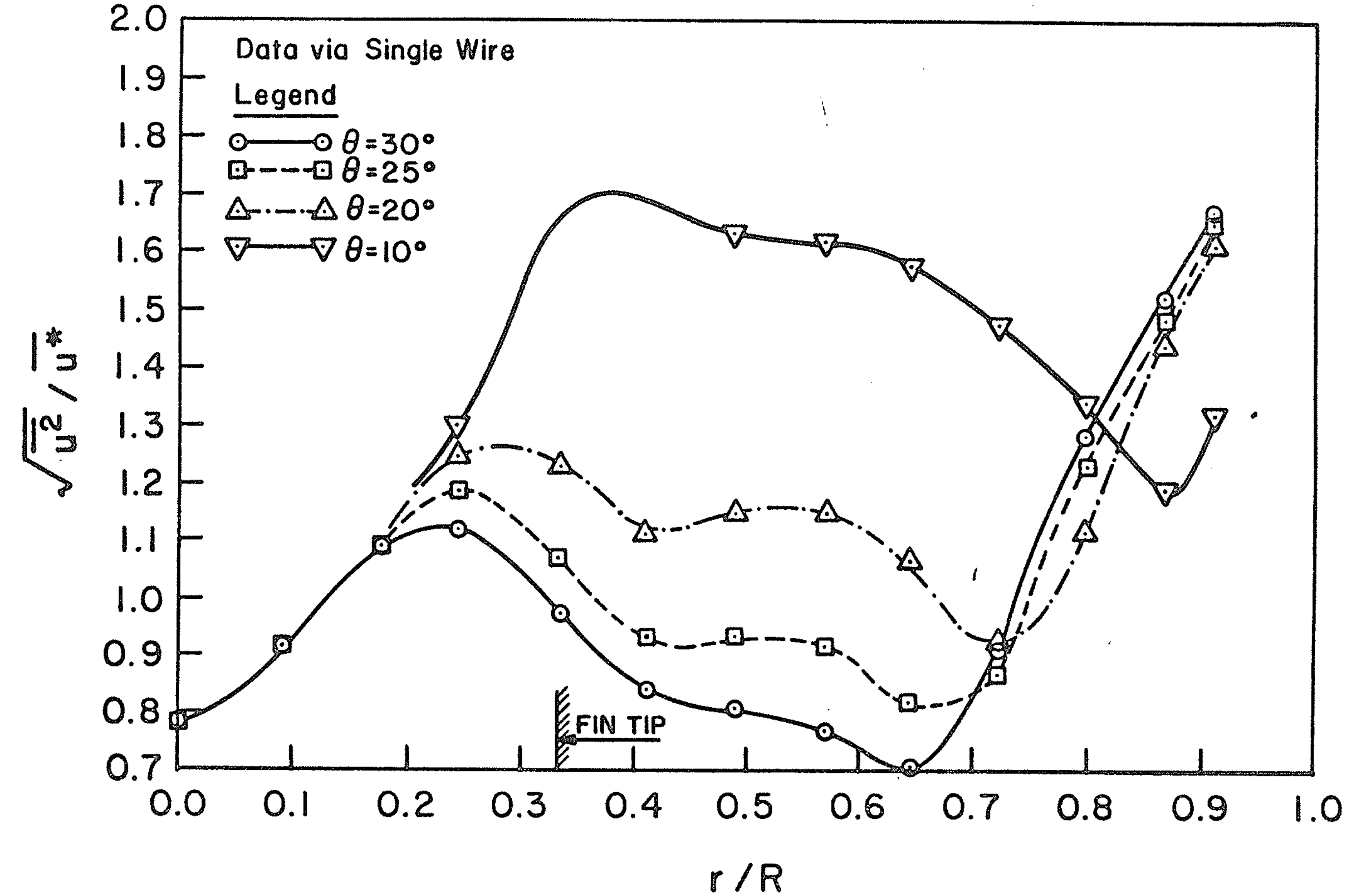

Figure 26: Radial Distribution of $\sqrt{\bar{u}^2}$ in Primary Flow Cell, Re = 71,000.

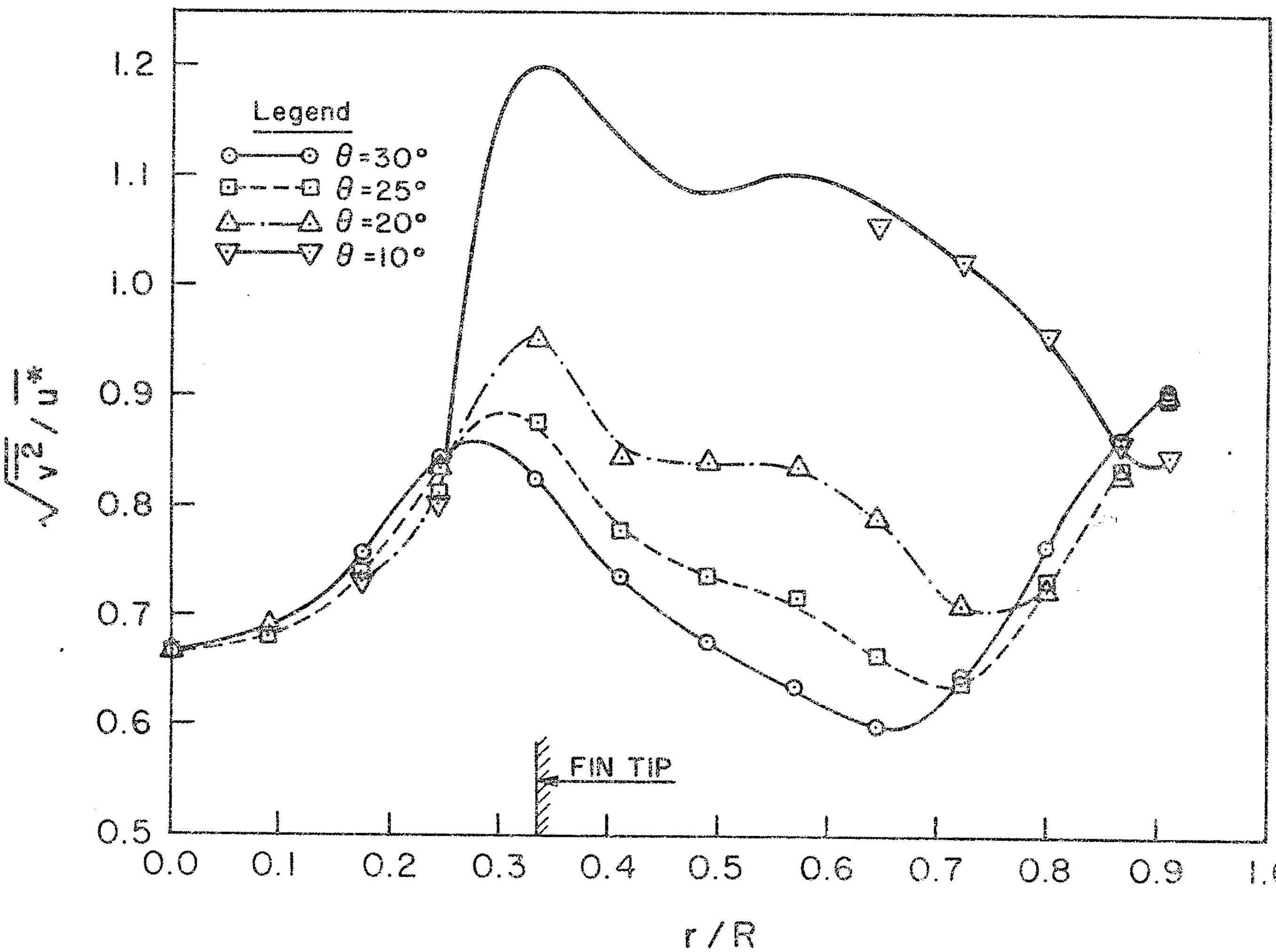

Figure 27: Radial Distributions of $\sqrt{\overline{v^2}}$ in Primary Flow Cell, Re = 71,000.

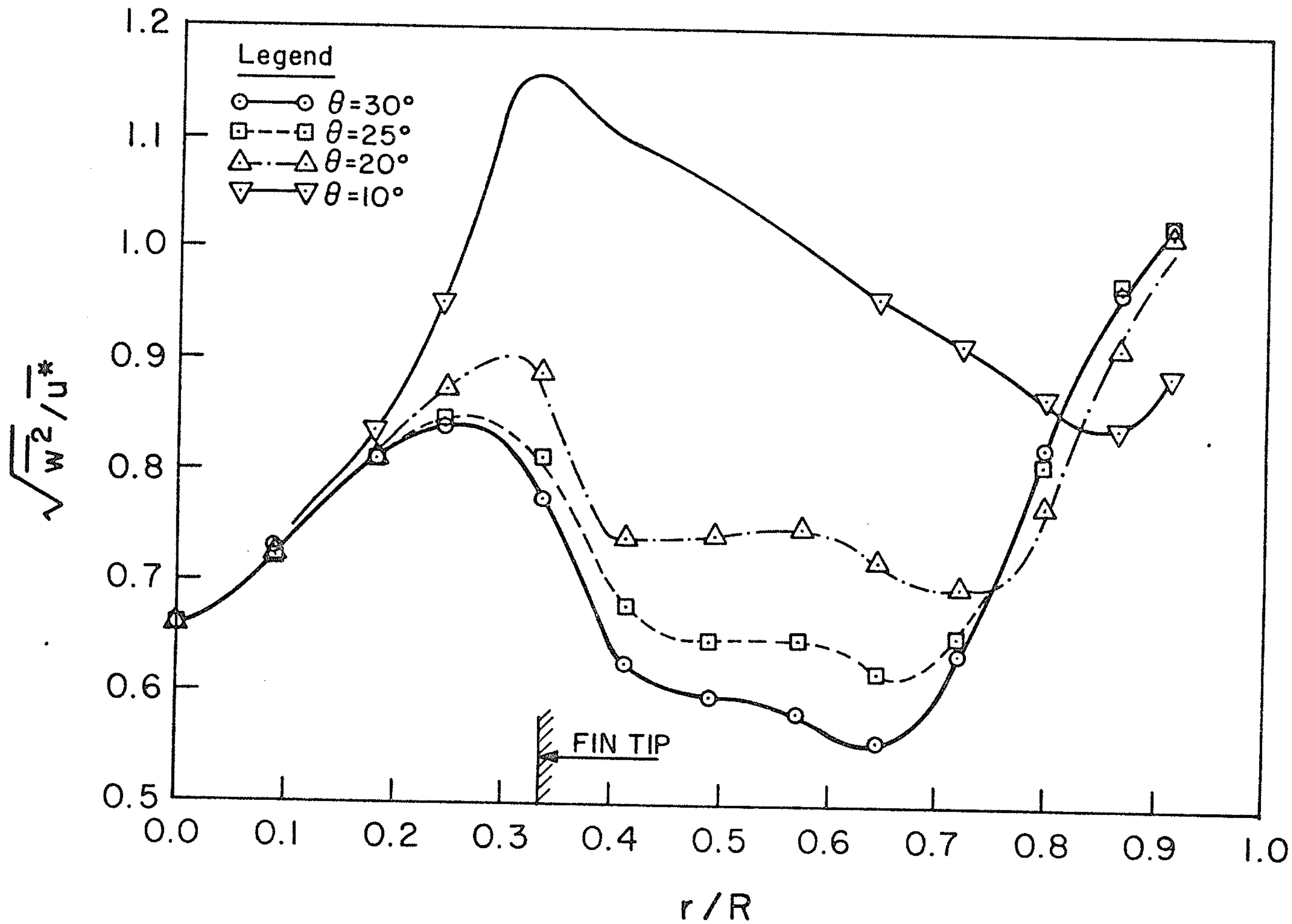

Figure 28: Radial Distributions of $\sqrt{\bar{w}^2}$ in Primary Flow Cell, Re = 71,000.

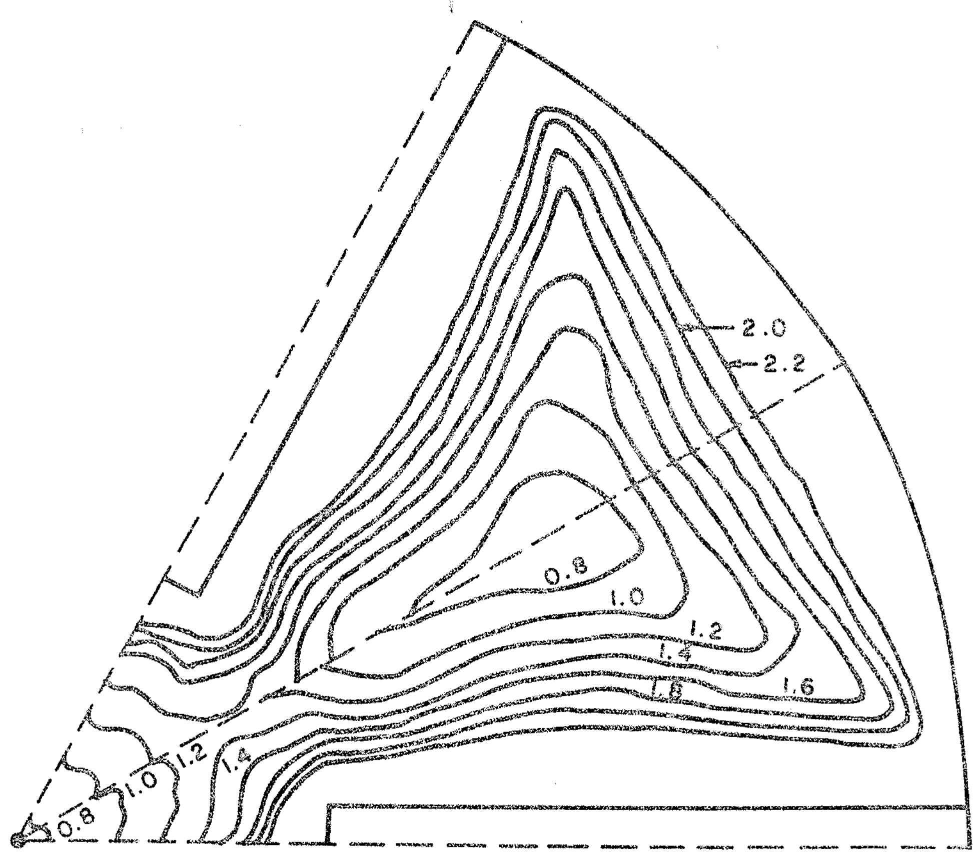

Figure 29: Turbulent Kinetic Energy Contours;Top - Re = 50,000, Bottom-Re = 71,000.

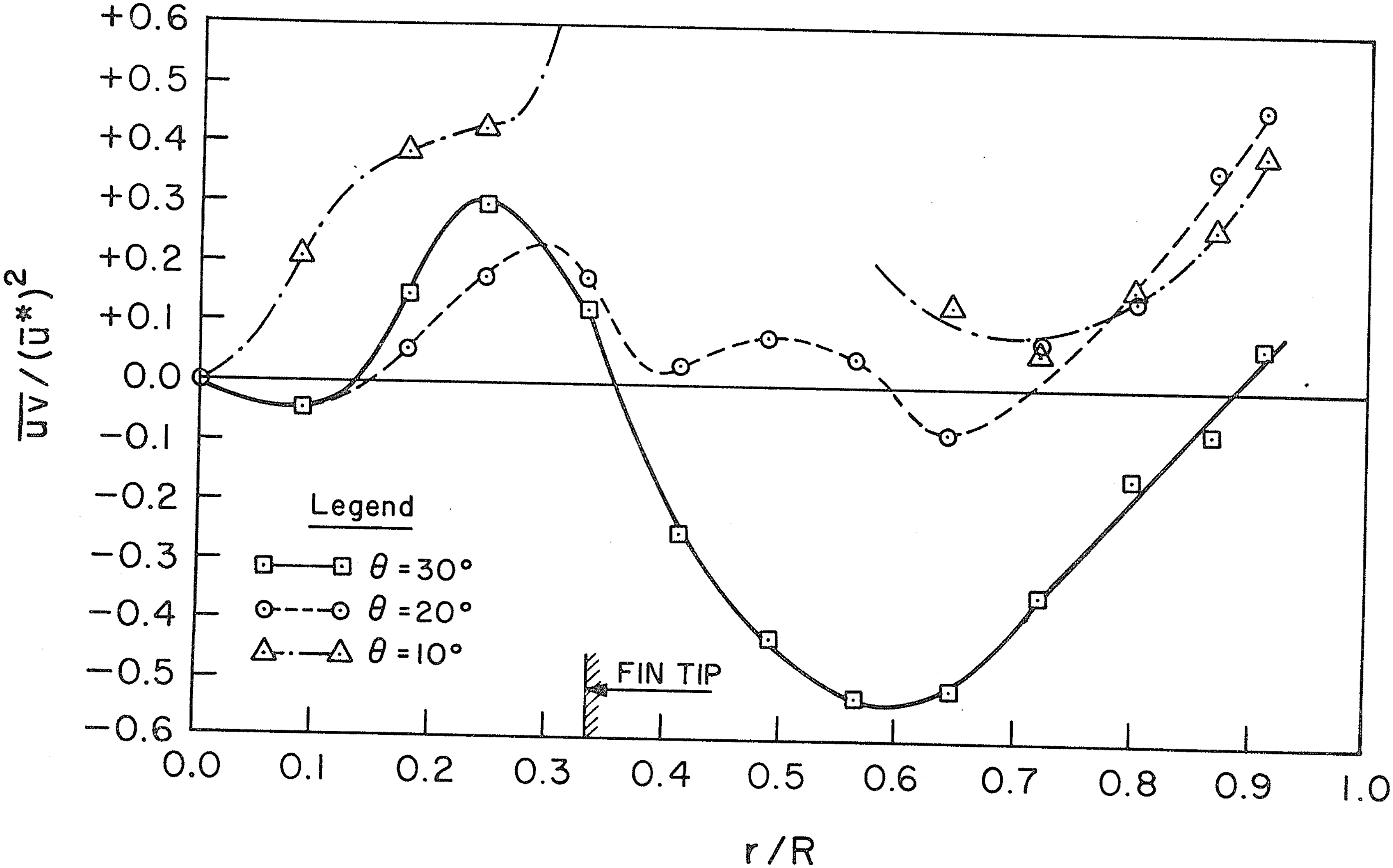

Figure 30: Radial Distributions of $\overline{uv}$ in Primary Flow Cell, Re = 71,000.

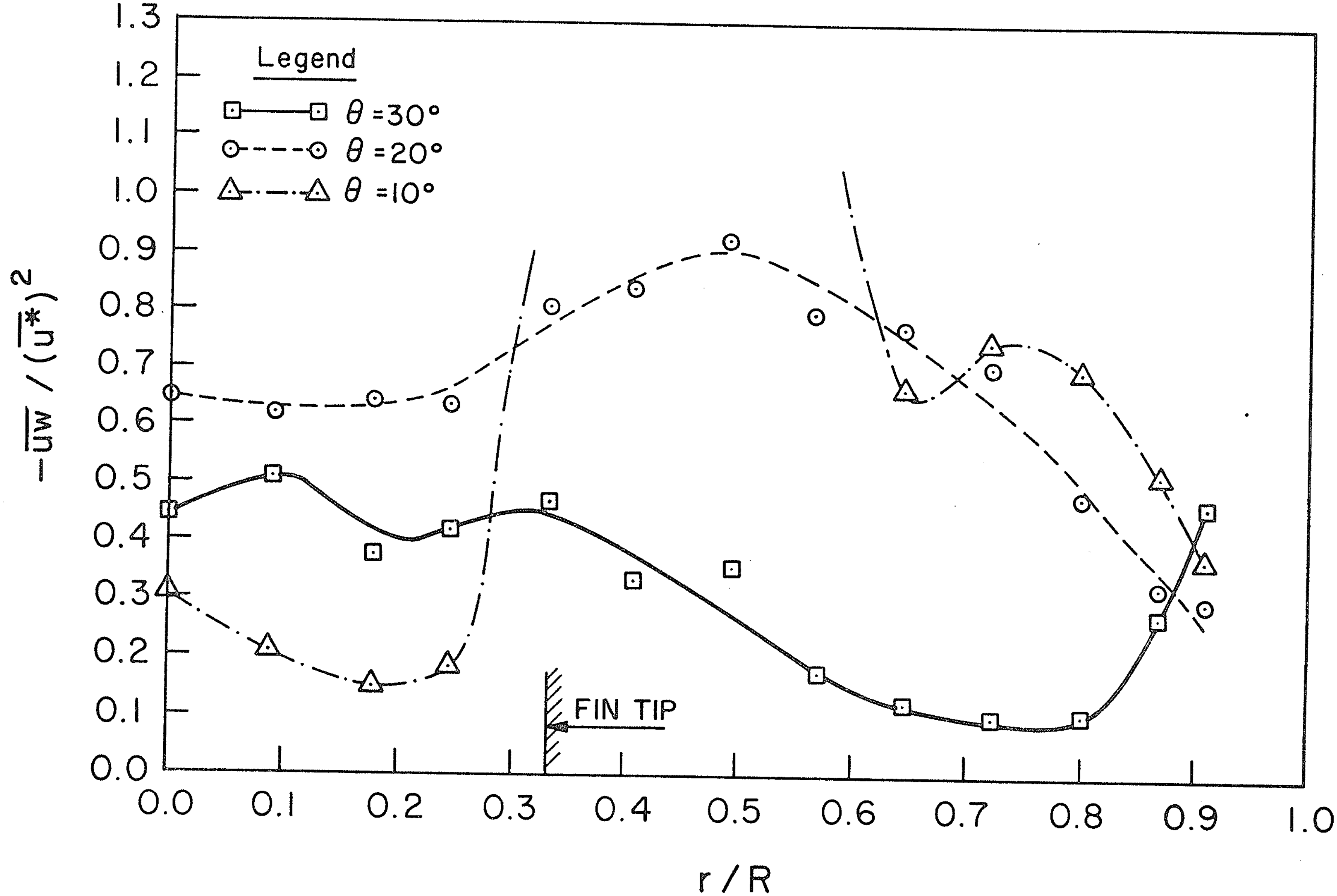

Figure 31: Radial Distribution of $\overline{uw}$ in Primary Flow Cell, Re = 71,000.

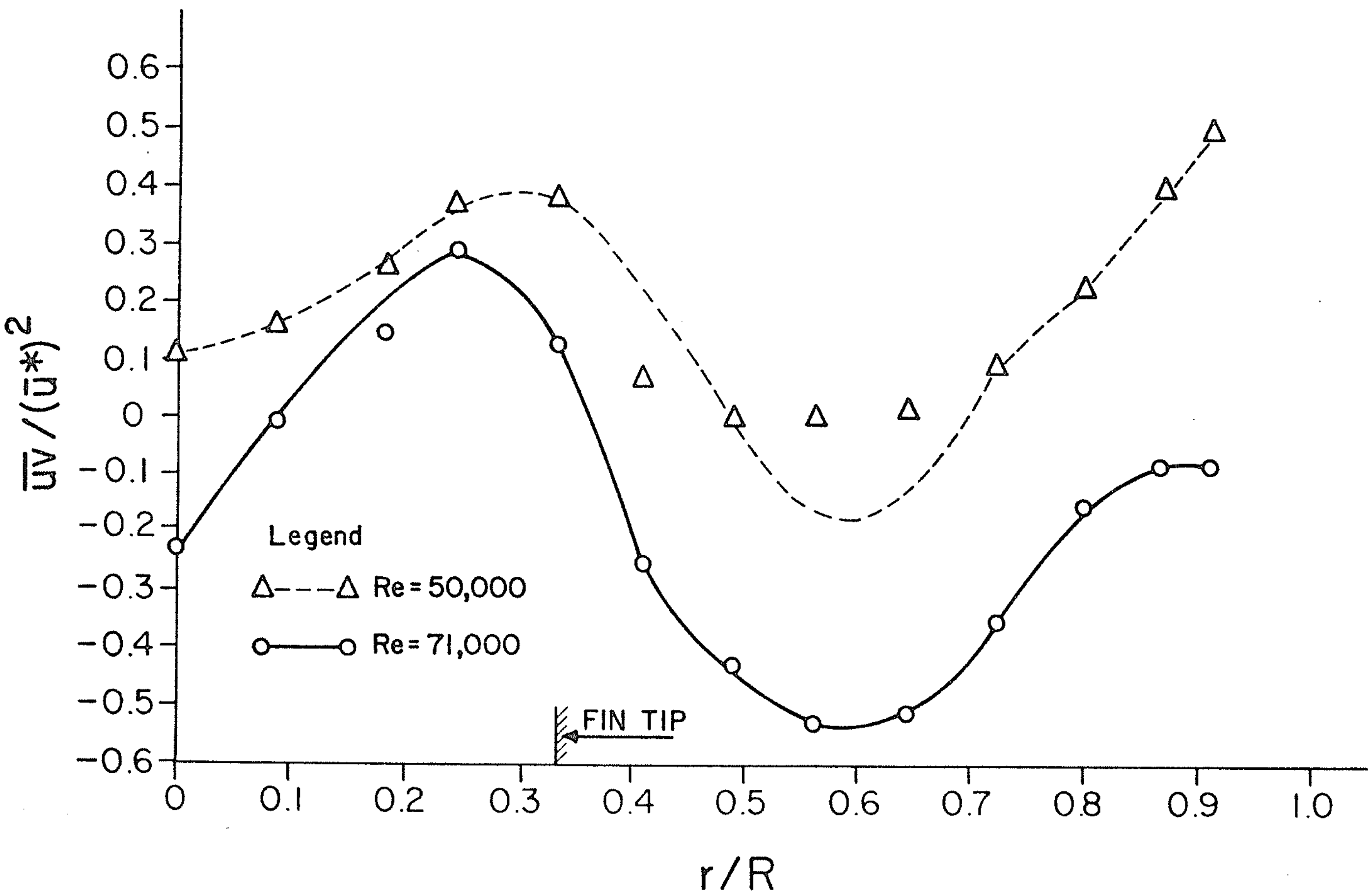

Figure 32: Radial Distribution of $\overline{uv}$, θ = 30°.

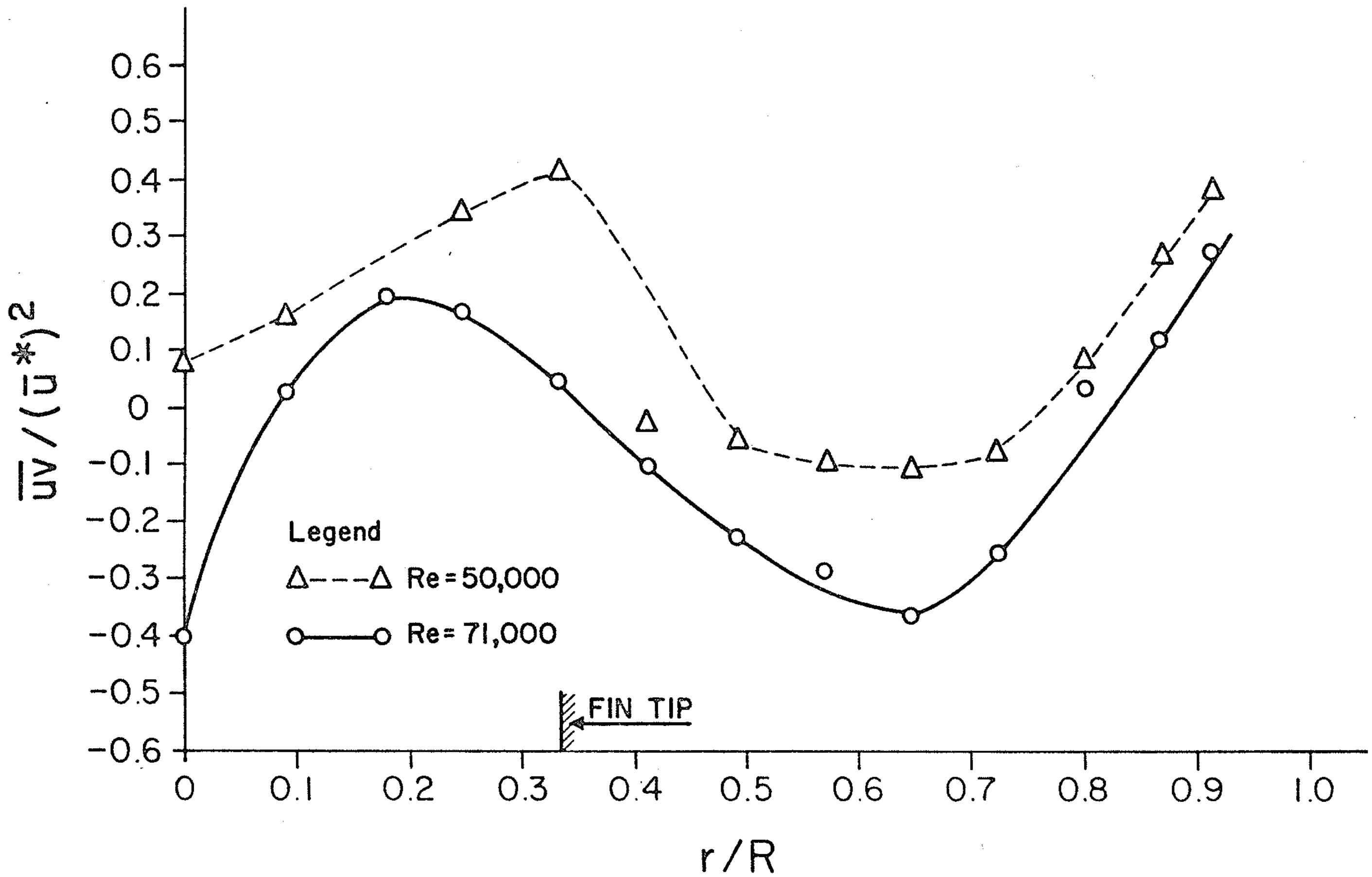

Figure 33: Radial Distribution of $\overline{uv}$, θ = 25°.

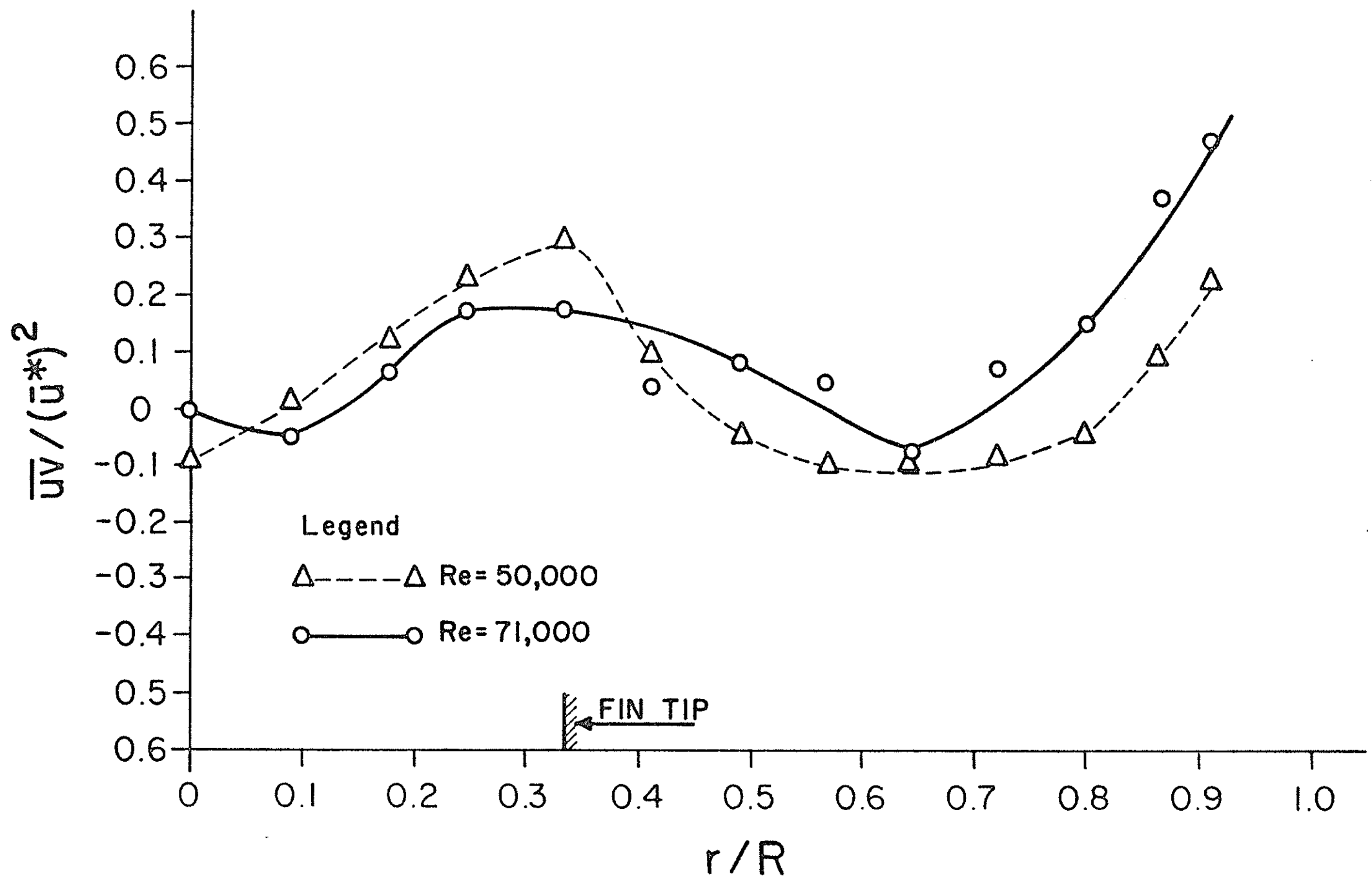

Figure 34: Radial Distribution of $\overline{uv}$, $\theta = 20°$.

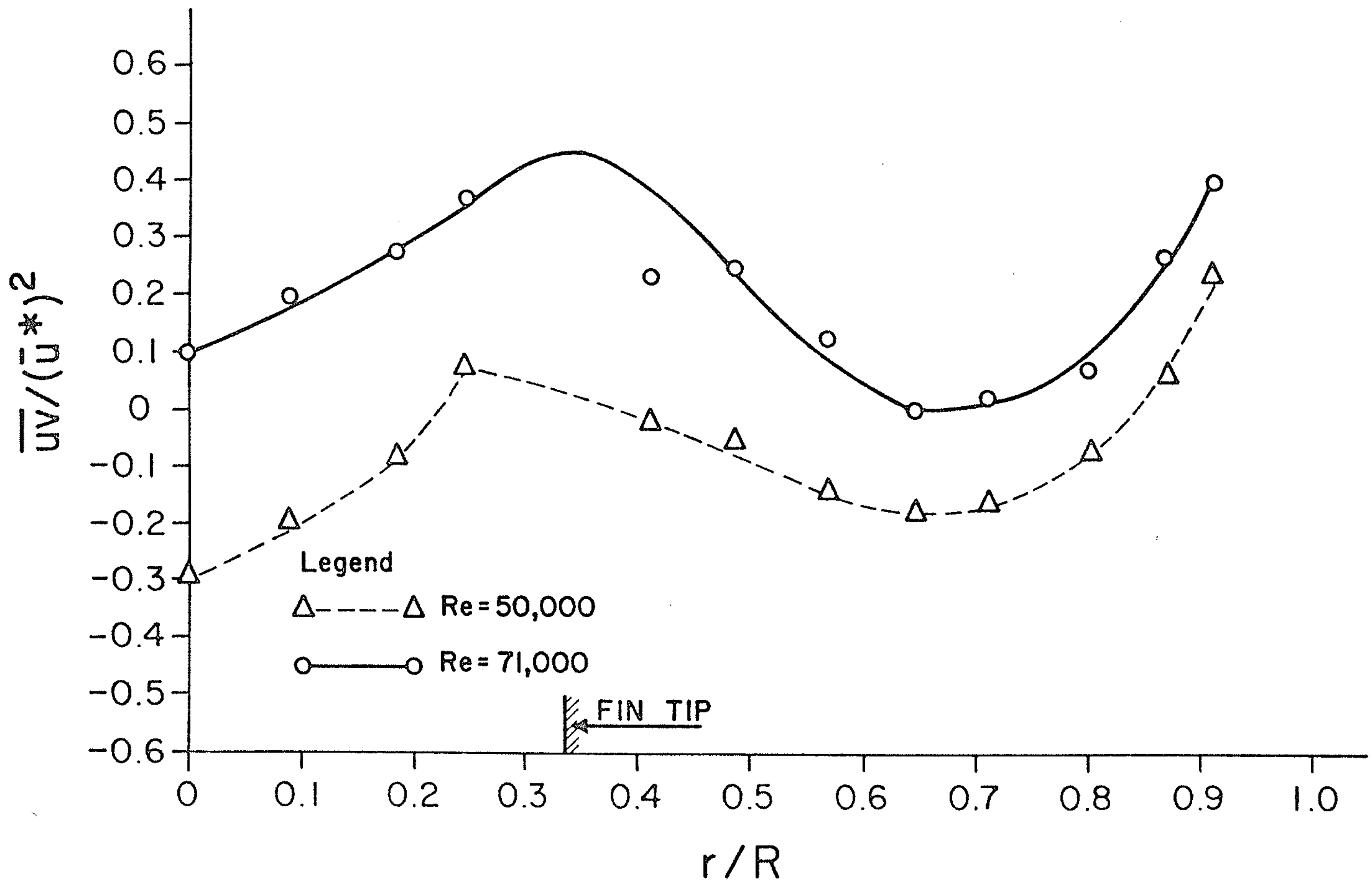

Figure 35: Radial Distribution of $\overline{uv}$, θ = 15°.

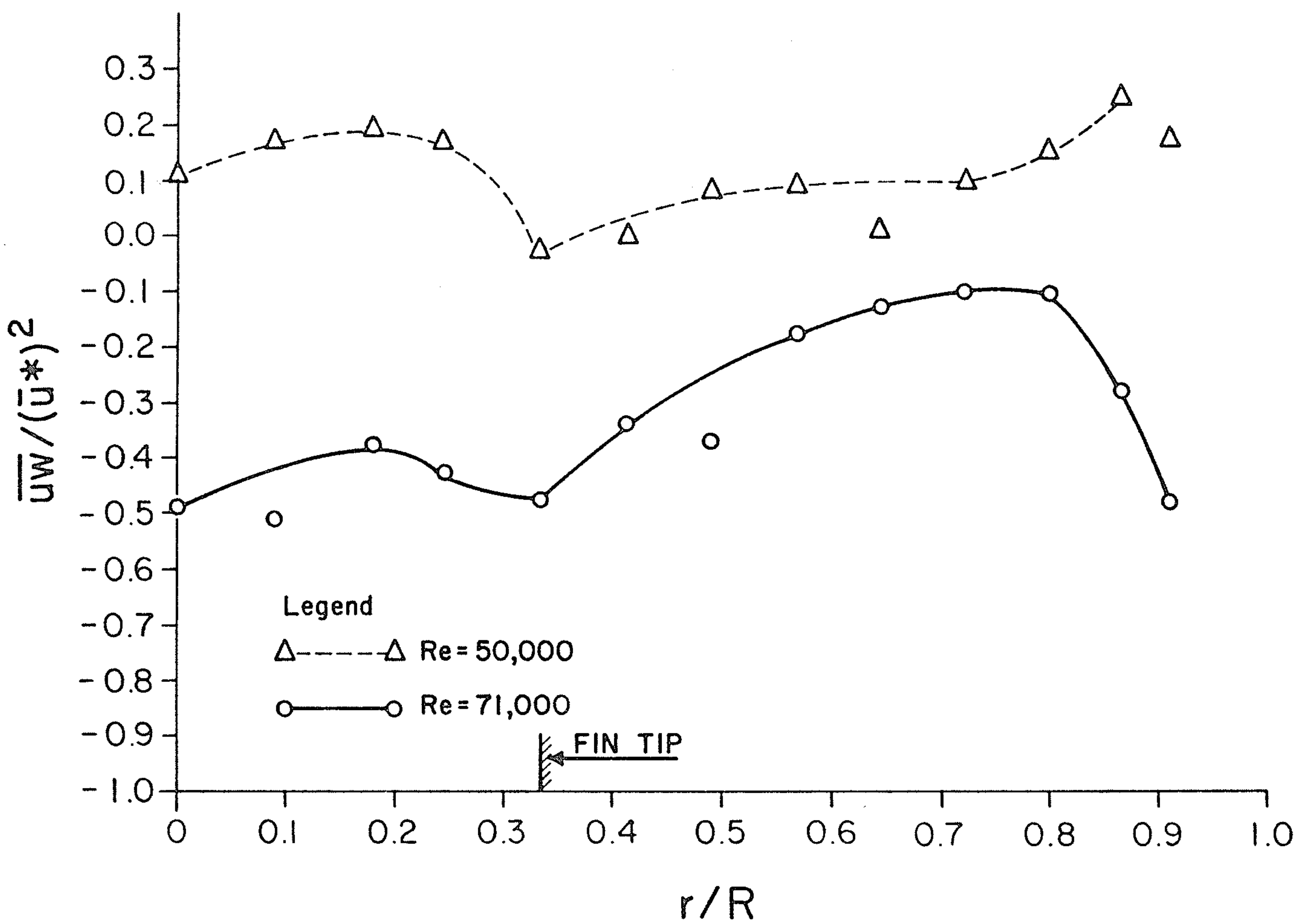

Figure 36: Radial Distribution of $\overline{uw}$, θ = 30°.

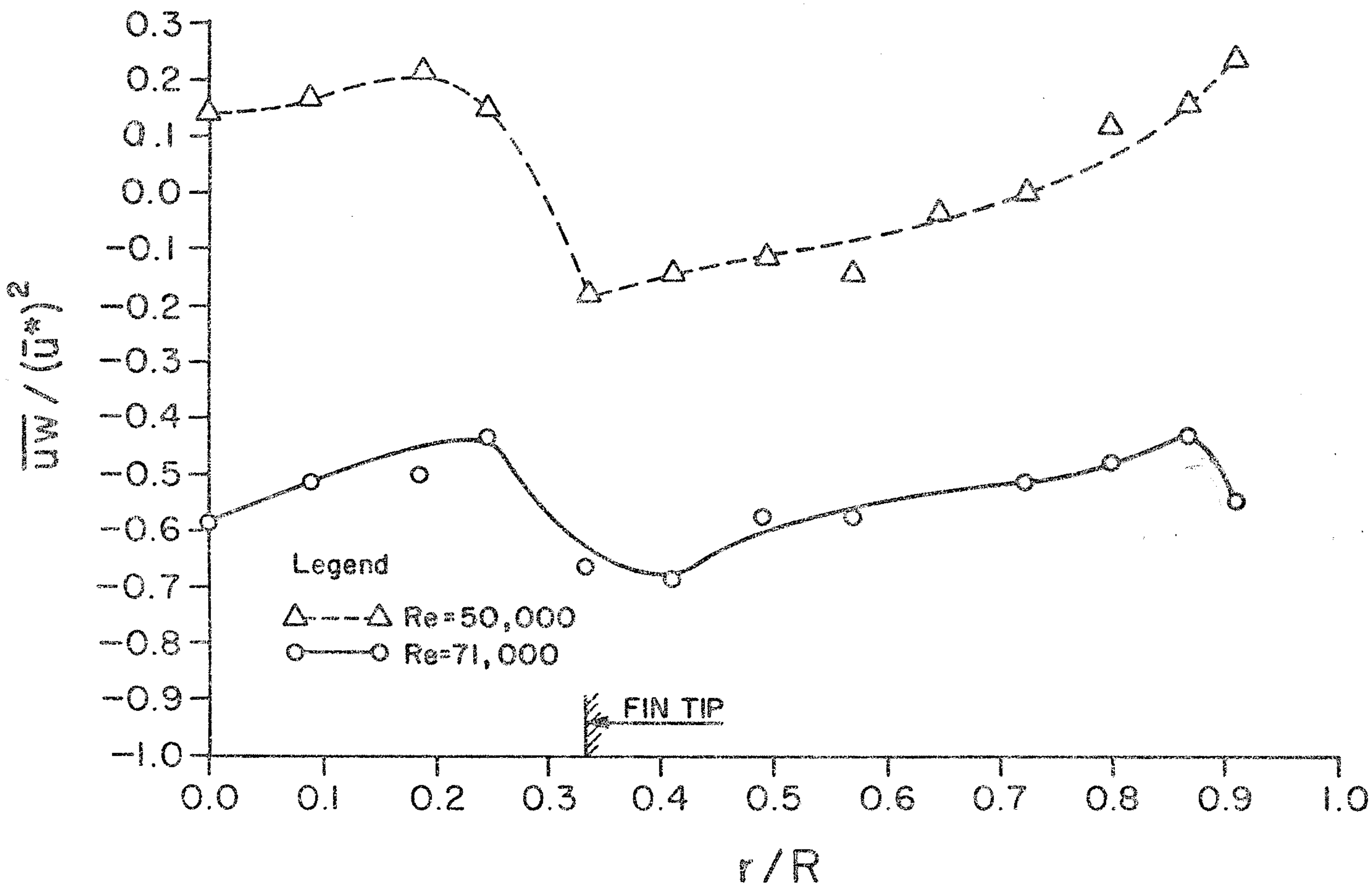

Figure 37: Radial Distribution of $\overline{uw}$, θ = 25°.

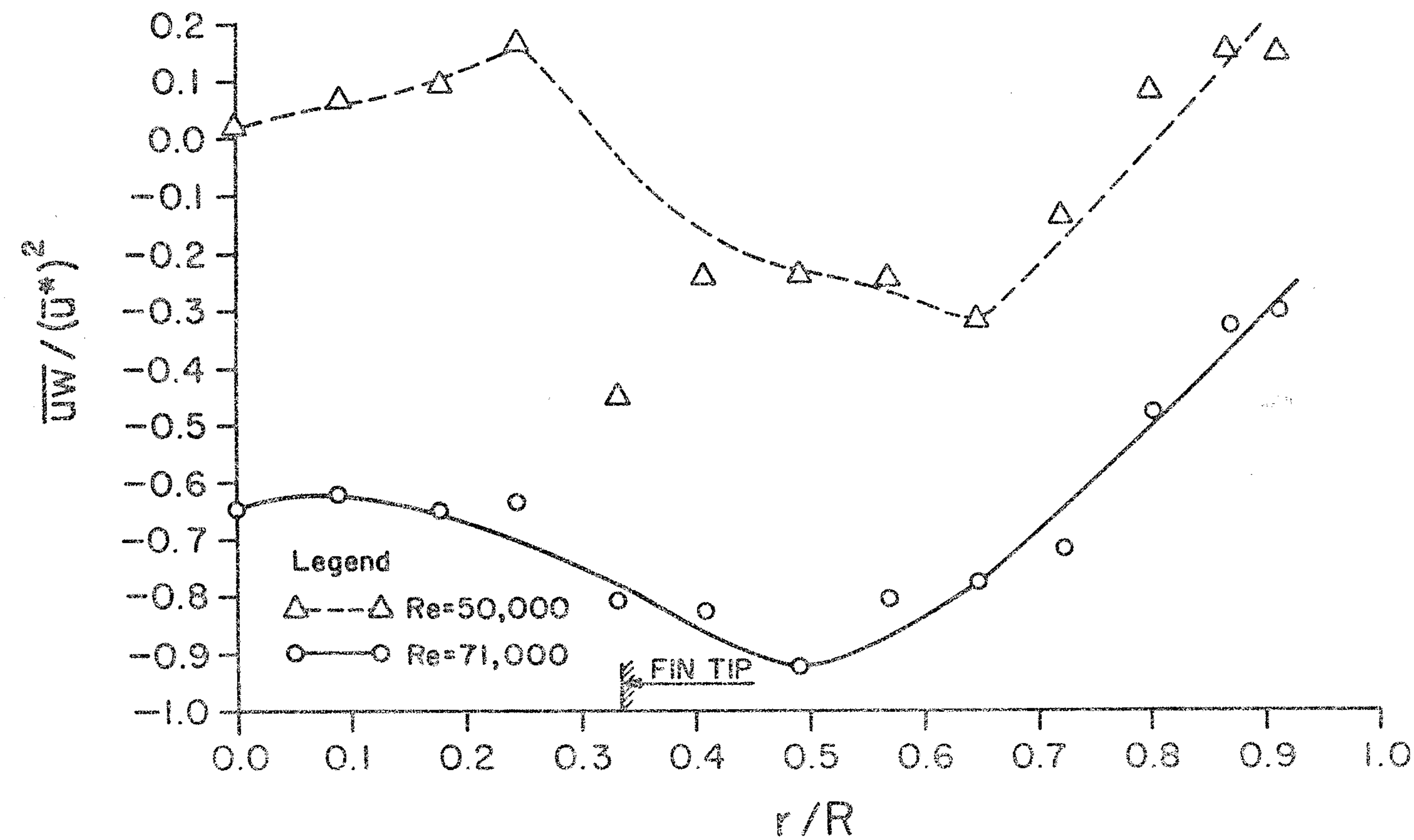

Figure 38: Radial Distribution of $\overline{uw}$, θ = 20°.

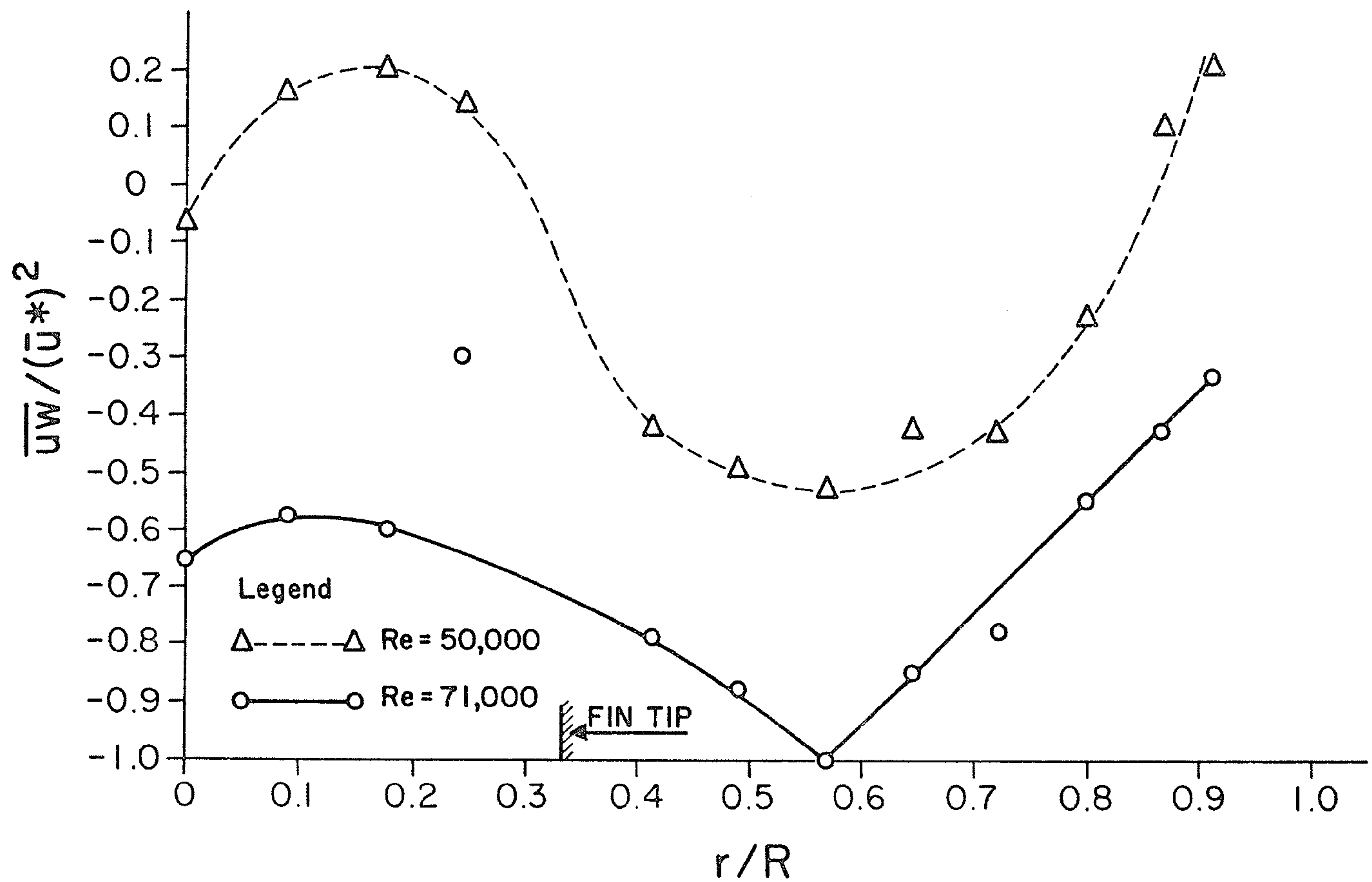

Figure 39: Radial Distribution of $\overline{uw}$, θ = 15°.